2016

Bondi Accretion in Trumpet Geometries

August J. Miller
Bowdoin College, amiller@bowdoin.edu

Bondi Accretion in Trumpet Geometries

An Honors Paper for the Department of Physics and Astronomy

By August J. Miller

Bowdoin College, 2016

Acknowledgments

First and foremost, I would like to thank my thesis advisor, Thomas Baumgarte, for his invaluable advice and help with this project. In addition, I would like to thank my major advisor, Madeleine Msall; Ken Dennison; and the rest of the Bowdoin College Department of Physics and Astronomy for helpful conversations and comments, and for their enormous contribution to and investment in my Bowdoin education. This work was supported in part by the NSF grant to Bowdoin College entitled "Numerical Simulations of Black Holes, Neutron Stars, and Gravitational Radiation."

Contents

List of Figures

List of Tables

Chapter 1

Introduction

Accretion of gas onto a black hole is an important and well-studied phenomenon in the field of relativistic astrophysics. In general, accretion processes are too complicated to describe analytically and require the use of a computer (see, e.g., [1] for a recent review). However, as was first demonstrated by Hermann Bondi in 1952, one simple case can be understood analytically, namely that of spherically symmetric, radial accretion onto a single, non-rotating black hole. Bondi considered fluid flow onto a point mass and, assuming conservation of mass and momentum, derived a set of equations relating the fluid density, velocity, sound speed, and radial distance. Bondi derived this solution assuming a Newtonian description of gravity; however, it was later re-derived in the context of relativistic gravity (see, e.g., [2,3], as well as Appendix G in [4] for a textbook treatment.) Both the Newtonian and relativistic solutions are referred to in the literature as Bondi solutions; the accretion process they describe is known as Bondi accretion. Despite their simplicity, these Bondi solutions have played an important role both in relativistic astrophysics, where they guide our understanding of more general accretion processes, and in numerical relativity, where they serve as well-understood test-cases for numerical codes. It is this second application that we will focus on here.

Many groups (e.g., [5–11]) have used Bondi accretion as a test-bed for numerical relativistic codes. One problem that must be addressed before the Bondi solution can be implemented numerically is the choice of coordinate system. The original Bondi solution is given in so-called Schwarzschild coordinates, the simplest mapping of the Schwarzschild

spacetime, i.e., the spacetime containing an isolated and non-rotating black hole. Unfortunately, these coordinates are not well-suited for numerical simulations. For one, simulations on a Cartesian grid require coordinate systems that are spatially isotropic, which Schwarzschild coordinates are not. Furthermore, Schwarzschild coordinates are singular on the black hole horizon, which introduces additional complications. Such issues can be avoided in codes that assume a fixed spacetime background by using, e.g., Kerr-Schild or ingoing Eddington-Finkelstein coordinates. However, in codes that evolve the matter and gravitational fields self-consistently, another solution is needed.

The first self-consistent evolutions of black hole spacetimes that did not rely on assumptions of symmetry were achieved by Pretorius [12], Campanelli et al. [13], and Baker et al. [14]. In the latter two publications the authors use an approach in which Einstein's equations, expressed in some variation of the Baumgarte-Shapiro-Shibata-Nakamura (BSSN) formulation [15–17] are evolved using so-called "moving-puncture" coordinates, which consist of a "1+log" slicing condition for the lapse [18] and a "Gamma-driver" condition for the shift vector [19]. As explained in greater detail in Section 4.1, the BSSN equations represent a reformulation of Einstein's equations in which the four-dimensional spacetime metric is decomposed into its spatial and time components; the lapse and shift encode coordinate conditions associated with this so-called $3+1$ decomposition. As described in [20, 21], moving-puncture coordinates act to bring the black hole initial data, which are expressed in isotropic Schwarzschild coordinates (see Section 4.3), into a so-called "trumpet" geometry (see [22] for a textbook treatment, as well as [23] for a simple analytical example). Spatial slices in trumpet coordinates are remarkable in that they penetrate the horizon of the black hole smoothly and end on a limiting surface with areal radius greater than zero, thereby "shielding" the simulation from the effects of the spacetime singularity.

One method by which the Bondi solution can be used as a test case for numerical codes that employ moving-puncture coordinates involves casting Bondi initial data into isotropic coordinates on slices of constant Schwarzschild time (see, e.g., [10]). Over the course of the evolution, the coordinate conditions described above act to bring the data into a trumpet geometry, which, thanks to the properties of trumpet coordinates, can

be handled numerically. While this is a proven method of simulating Bondi accretion, it has several disadvantages. First of all, because isotropic Schwarzschild coordinates cover only the region of the Schwarzschild spacetime corresponding to $R > 2GM/c^2$ (i.e., the region outside the horizon), it is necessary to specify artificial initial data inside this limit. Second, and more importantly, the fact that the coordinates themselves transform during the course of the evolution means that only gauge-independent quantities can be compared directly with the analytical Bondi solution.

Here we show that it is possible, and in fact quite straightforward, to transform the original Bondi solution into coordinates with a trumpet geometry. We then use a numerical code that implements the BSSN formulation of Einstein's equations, together with moving-puncture coordinates, to evolve this solution forward in time, and demonstrate that it remains time-independent. As a result, all quantities, not just those that are gauge-invariant, can be compared with the analytical solution. Furthermore, casting the Bondi solution in trumpet coordinates eliminates the need for artificial initial data in the vicinity of the puncture, since the Bondi solution now extends smoothly into the black hole interior.

We organize our discussion as follows. In Chapter 2 we reproduce Bondi's original derivation in the Newtonian approximation. Next, in Chapter 3, we derive the analogous solution in relativistic gravity; this is the solution that we will use in the rest of our calculations. In Chapter 4 we describe how to transform the Bondi solution in Schwarzschild coordinates into the three coordinate systems we will consider in our numerical simulations: isotropic coordinates on slices of constant Schwarzschild time, maximal trumpet coordinates, and analytical trumpet coordinates. We present our numerical results for each of these coordinate systems in Chapter 5, and conclude with a brief summary in Chapter 6.

Chapter 2

Bondi accretion onto a black hole: The Newtonian equations

In this section we derive Bondi's solution for spherically symmetric, radial flow onto a point mass. We assume the density is small enough that the self-gravity of the fluid is negligible. We can choose to think of this solution as representing the flow onto a stationary, non-rotating black hole in the Newtonian limit. As may be expected, the Newtonian solution does not accurately describe the fluid behavior at small radii. A correct description that extends to the event horizon of the black hole can only be obtained through a relativistic treatment. However, at large radii $r \gg 2GM/c^2$, the Newtonian solution offers a good approximation. Furthermore, the structure of the Newtonian solution, as it is presented below, provides a useful template for the more complicated relativistic solution, which is presented in Chapter 3. We will see that many of the key equations in this section have close analogues in the relativistic solution, and we will reference the corresponding equation in the other section whenever this is the case. All quantities in this chapter are expressed in SI units.

The following discussion closely follows that presented in Section 14.3 of Shapiro and Teukolsky [4]. We will reference equations in that text using the notation ST.#, where # is the corresponding equation number [e.g., Eq. (ST.14.3.1)].

2.1 Derivation of the fluid equations

We start by assuming the accreting gas to be adiabatic to first approximation. As discussed in greater detail in the following chapter, this implies that the pressure P is related to the density ρ of the gas by a polytropic equation of state

$$P = \kappa \rho^{\Gamma} \tag{2.1}$$

[cf. Eq. (ST.14.3.1)], where κ is known as the polytropic constant and Γ is the adiabatic index. The sound speed a, which will enter later in our discussion, is given by

$$a = \left(\frac{dP}{d\rho}\right)^{1/2} = \left(\Gamma \kappa \rho^{\Gamma-1}\right)^{1/2} = \left(\frac{\Gamma P}{\rho}\right)^{1/2}. \tag{2.2}$$

We use spherical polar coordinates and assume radial flow with velocity $\mathbf{u} = (u^r, 0, 0)$. Since we are considering accretion onto the black hole, we have $u^r \leq 0$ always. For convenience, we define the inward radial velocity of the fluid as $u \equiv -u^r$. We further assume that the gas is at rest ($u = 0$) at $r = \infty$, and denote the pressure, density, and sound speed at infinity as P_∞, ρ_∞, and $a_\infty = (\Gamma P_\infty/\rho_\infty)^{1/2}$, respectively.

The fluid flow is completely governed by three equations, namely the equation of state (2.1); the continuity equation,

$$\nabla \cdot (\rho \mathbf{u}) = \frac{1}{r^2}\frac{d}{dr}\left(r^2 \rho u\right) = 0 \tag{2.3}$$

[cf. Eq. (ST.14.3.2)], which expresses conservation of mass; and the Euler equation,

$$u\frac{du}{dr} = -\frac{1}{\rho}\frac{dP}{dr} - \frac{GM}{r^2} \tag{2.4}$$

[cf. Eq. (ST.14.3.3)], which expresses conservation of momentum. Note that Eqs. (2.3) and (2.4) hold only for $r > 0$. Here G is the gravitational constant and M is the mass of the black hole. As mentioned above, we assume the density of the gas to be small enough that we can neglect self-gravity. We find it useful to rewrite the continuity equation (2.3)

in a slightly different form. Carrying out the total derivative yields

$$\frac{1}{r^2}\frac{d}{dr}\left(r^2\rho u\right) = \frac{1}{r^2}\left(2r\rho u + r^2\rho' u + r^2\rho u'\right) = \frac{2\rho u}{r} + \rho' u + \rho u' = 0, \tag{2.5}$$

where in the last equality we have introduced $\rho' \equiv d\rho/dr$ and $u' \equiv du/dr$. Dividing all terms by ρu, we obtain

$$\frac{\rho'}{\rho} + \frac{u'}{u} + \frac{2}{r} = 0 \tag{2.6}$$

[cf. Eq. (ST.14.3.6)]. We will refer to Eq. (2.6) as the first Newtonian fluid equation. We can similarly rewrite Eq. (2.4) to eliminate dependence on the pressure P. From Eqs. (2.1) and (2.2), we have

$$\frac{dP}{dr} = \frac{dP}{d\rho}\frac{d\rho}{dr} = a^2\rho', \tag{2.7}$$

which, when substituted into Eq. (2.4), yields

$$uu' + a^2\frac{\rho'}{\rho} + \frac{GM}{r^2} = 0 \tag{2.8}$$

[cf. Eq. (ST.14.3.7)]. We designate Eq. (2.8) the second Newtonian fluid equation.

2.2 Solution at the critical radius

Equations (2.6) and (2.8) can now be solved for the radial derivatives u' and ρ'. Combining the two equations to eliminate ρ yields

$$uu' - a^2\left(\frac{u'}{u} + \frac{2}{r}\right) + \frac{GM}{r^2} = 0, \tag{2.9}$$

which can be rearranged to find

$$u' = u\left(\frac{2a^2/r - GM/r^2}{u^2 - a^2}\right). \tag{2.10}$$

Inserting (2.10) into (2.6) gives

$$\frac{\rho'}{\rho} = -\frac{2a^2/r - GM/r^2}{u^2 - a^2} - \frac{2}{r}, \tag{2.11}$$

or

$$\rho' = -\rho\left(\frac{2u^2/r - GM/r^2}{u^2 - a^2}\right). \tag{2.12}$$

Finally, we can rewrite Eqs. (2.10) and (2.12) as

$$u' = \frac{D_1}{D}, \qquad \rho' = -\frac{D_2}{D} \tag{2.13}$$

[cf. Eq. (ST.14.3.8)], where we have defined

$$D_1 \equiv \frac{2a^2/r - GM/r^2}{\rho}, \tag{2.14}$$

$$D_2 \equiv \frac{2u^2/r - GM/r^2}{u}, \tag{2.15}$$

and

$$D \equiv \frac{u^2 - a^2}{\rho u} \tag{2.16}$$

[cf. Eqs. (ST.14.3.9), (ST.14.3.10), and (ST.14.3.11), respectively].

Now, since the flow is subsonic ($u < a$) at $r = \infty$ and supersonic ($u > a$) close to the black hole, and we are assuming u increases monotonically as we move inward from infinity, then somewhere in between it must pass through a critical point where $u = a$. We call this point, which marks the transition between subsonic and supersonic flow, the *transonic* point. The radius at which it occurs is known as the critical or sonic radius, denoted r_s. From Eq. (2.16), we see that $u = a$ implies $D = 0$. Since the radial derivatives of the density and velocity [Eq. (2.13)] must remain finite for all r, we must have $D_1 = D_2 = D = 0$ at $r = r_s$ [cf. Eq. (ST.14.3.12)].

We can use this condition to calculate the fluid velocity and the sound speed at the transonic point in terms of the sonic radius. From (2.15) we have

$$\frac{2u_s^2}{r_s} - \frac{GM}{r_s^2} = 0, \tag{2.17}$$

where the s subscript indicates that the quantity is being evaluated at $r = r_s$. Rearranging yields

$$u_s^2 = a_s^2 = \frac{1}{2}\frac{GM}{r_s}. \tag{2.18}$$

[cf. Eq. (ST.14.3.13)]. (Note that the same result can be found by solving the equation $D_1 = 0$ for a_s.)

2.3 Conservation equations

We conclude our derivation by recasting the continuity equation (2.3) and the Euler equation (2.4) in the form of conservation equations. We begin by recognizing that the accretion rate, i.e., the flux of the gas through a spherical surface of radius r, is equal to the area of that surface ($4\pi r^2$) multiplied by the flux density of the gas (ρu). Since, by Eq. (2.3), the quantity $r^2\rho u$ is constant with respect to r, the accretion rate, which we denote $\dot{M}$, must be constant as well. We therefore have

$$4\pi\rho u r^2 = \text{constant} = \dot{M} \tag{2.19}$$

[cf. Eq. (ST.14.3.4)], where we have defined $\dot{M}$ to be positive for ingoing flow ($u > 0$). Eq. (2.4) can likewise be integrated to obtain an equation relating the velocity u and the sound speed a. We start by rewriting Eq. (2.4) as

$$u du = -\frac{dP}{\rho} - \frac{GM}{r^2}dr, \tag{2.20}$$

or, using (2.1) to eliminate the dependence on P,

$$u du + \Gamma\kappa\rho^{\Gamma-2}d\rho + \frac{GM}{r^2}dr = 0. \tag{2.21}$$

Integrating this equation yields

$$\frac{u^2}{2} = -\frac{\Gamma\kappa\rho^{\Gamma-1}}{\Gamma-1} + \frac{GM}{r} + C, \tag{2.22}$$

where C is a constant of integration. We can rewrite the second term in terms of the sound speed a to obtain

$$\frac{1}{2}u^2 + \frac{1}{\Gamma-1}a^2 - \frac{GM}{r} = C. \tag{2.23}$$

Eq. (2.23) must hold for all values of the radius r. We can therefore determine the value of C by evaluating the left-hand side in the limit $r \to \infty$ ($u \to 0$), which yields

$$\frac{1}{2}u^2 + \frac{1}{\Gamma-1}a^2 - \frac{GM}{r} = \frac{1}{\Gamma-1}a_\infty^2 \tag{2.24}$$

[cf. Eq. (ST.14.3.5)]. Eq. (2.24) is known as the Bernoulli equation.

In his original analysis, Bondi [24] showed that different values of $\dot{M}$ lead to distinct classes of solutions to the fluid equations (2.6) and (2.8) for the same boundary conditions at infinity (i.e., the same values of P_∞, ρ_∞, and a_∞). In this chapter, we have limited our discussion to the unique solution for which the velocity increases monotonically from $u = 0$ at $r = \infty$ to the free-fall velocity at small radii [$u \to (2GM/r)^{1/2}$ as $r \to 0$]. As we will see in Chapter 3, the relativistic equations for accretion onto a black hole demand that we choose this solution in order to avoid singularities in the flow outside the event horizon.

At this point we have derived all of the key components of Bondi's solution for spherically symmetric, radial accretion onto a point mass. In Appendix A, we derive, for completeness, the equation for the accretion rate in terms of the boundary values at infinity, as well as the flow profiles in the limits $r \gg r_s$ and $r \ll r_s$, but this information is not relevant to the rest of our analysis. It is important to note that nowhere in the above discussion did we actually write down equations for the density and velocity of the fluid as functions of r. This is because, as we will see again in the relativistic case, such functions cannot be expressed analytically. In order to find $\rho(r)$, for example, we must

compute ρ iteratively for discrete values of r, and then assemble the resulting values into a radial profile.

Chapter 3

Bondi accretion onto a black hole: The relativistic equations

In the previous chapter we derived Bondi's equations for spherically symmetric, adiabatic accretion onto a black hole in the Newtonian limit. We now derive an analogous set of equations assuming a relativistic description of gravity. We assume throughout our derivation that the self-gravity of the accreting gas (i.e., the warping effect of the gas on the background spacetime) is negligible. We also ignore any increase in mass of the black hole due to the inflow of matter over time. One additional subtlety that arises in the relativistic treatment is that we must now be careful to distinguish between the total density of the fluid, denoted ρ, and the proper rest-mass density (i.e., the rest-mass density as measured by an observer comoving with the fluid), denoted ρ_0. We define ρ as the sum of ρ_0 and the internal energy density of the fluid:

$$\rho = \rho_0 + \varepsilon \tag{3.1}$$

[cf. Eq. (ST.G.1)]. In the Newtonian approximation, ρ and ρ_0 are assumed to be equal, since the internal energy density of the fluid is negligible by comparison. At infinity, the gas has rest-mass density $\rho_{0,\infty}$ and total density ρ_∞. Here and in the rest of this thesis we use geometrized units ($c = G = 1$).

3.1 Derivation of the fluid equations

We will derive the relativistic Bondi solution from two key equations. The first of these equations is the law of baryon conservation,

$$\nabla_a \left(\rho_0 u^a\right) = 0 \tag{3.2}$$

[cf. Eq. (ST.G.2)], where $u^a = \left(u^t, u^R, 0, 0\right)$ is the four-velocity of the fluid and ∇_a represents the covariant derivative associated with the spacetime metric g_{ab}. The Newtonian analogue of this equation is the continuity equation, Eq. (2.3). The second key equation is the conservation of energy-momentum,

$$\nabla_b T^{ab} = 0, \tag{3.3}$$

where T^{ab} is the stress-energy tensor for a perfect fluid,

$$T^{ab} = \left(\rho + P\right) u^a u^b + P g^{ab}. \tag{3.4}$$

Eq. (3.3) is a vector equation; as shown in Appendix C, the spatial part of this equation can be rewritten as

$$\left(\rho + P\right) u^b \nabla_b u^a = -\partial^a P - u^a u^b \partial_b P \tag{3.5}$$

[cf. Eq. (ST.G.3)], where P is the pressure of the gas. Eq. (3.5) is known as the relativistic Euler equation and expresses the conservation of momentum. If we instead evaluate the time component of Eq. (3.3), we obtain the entropy equation,

$$d\left(\frac{\epsilon}{\rho_0}\right) = -P d\left(\frac{1}{\rho_0}\right) \tag{3.6}$$

[cf. Eq. (ST.G.4)]. Eq. (3.6) is a statement of the first law of thermodynamics with the condition that the entropy is constant. We therefore conclude that the flow must be

adiabatic in the absence of shocks. We will later find it useful to rewrite Eq. (3.6) as

$$\frac{d\rho}{d\rho_0} = \frac{\rho + P}{\rho_0} \tag{3.7}$$

[cf. Eq. (ST.G.5)]. [For a complete derivation of Eqs. (3.6) and (3.7), see Appendix D.] We adopt a Gamma-law equation of state for the accreting fluid, in which the pressure P is given by

$$P = (\Gamma - 1)\,\varepsilon, \tag{3.8}$$

where Γ is the adiabatic index and ε is the internal energy density of the fluid [see Eq. (3.1)]. We will proceed to show that this choice of the equation of state, when combined with the entropy equation (3.6), yields a polytropic relation between P and ρ_0 [see Eq. (3.14)]. We begin by rewriting Eq. (3.6) as

$$\frac{1}{\rho_0} d\varepsilon - \frac{\varepsilon}{\rho_0^2} d\rho_0 = \frac{P}{\rho_0^2} d\rho_0, \tag{3.9}$$

which simplifies to

$$\rho_0 d\varepsilon = (\varepsilon + P)\, d\rho_0, \tag{3.10}$$

or

$$\frac{d\varepsilon}{\varepsilon + P} = \frac{d\rho_0}{\rho_0}. \tag{3.11}$$

Using our equation of state (3.8), we can rewrite this as

$$\left(\frac{1}{\Gamma - 1}\right)\left(\frac{dP}{P/(\Gamma - 1) + P}\right) = \frac{dP}{\Gamma P} = \frac{d\rho_0}{\rho_0}. \tag{3.12}$$

Integrating this equation yields

$$\frac{1}{\Gamma} \ln P = \ln \rho_0 + C, \tag{3.13}$$

or

$$P = \kappa \rho_0^{\Gamma}, \tag{3.14}$$

where κ is known as the polytropic constant [cf. Eq. (2.1)].

In order to proceed with our derivation, we must choose a coordinate system. Following the example in [24], we will derive the Bondi equations in Schwarzschild coordinates, in which the line element is given by

$$ds^2 = -\left(1 - \frac{2M}{R}\right) dt^2 + \left(1 - \frac{2M}{R}\right)^{-1} dR^2 + R^2 d\Omega^2, \tag{3.15}$$

where t is the Schwarzschild time, R is the Schwarzschild radius, and M is the mass of the black hole; the event horizon of the black hole is located at $R = 2M$. We can now evaluate Eqs. (3.2) and (3.5) in these coordinates to obtain the relativistic fluid equations. Eq. (3.2) evaluated in Schwarzschild coordinates yields

$$\frac{{\rho_0}'}{\rho_0} + \frac{u'}{u} + \frac{2}{R} = 0, \tag{3.16}$$

[cf. Eq. (ST.G.6)], which is easily recognizable as the relativistic analogue of Eq. (2.6). Eq. (3.5), on the other hand, yields

$$uu' = -\frac{1}{\rho + P}\frac{dP}{dR}\left(1 - \frac{2M}{R} + u^2\right) - \frac{M}{R^2}, \tag{3.17}$$

which corresponds to Eq. (2.4). [For complete derivations of Eqs. (3.16) and (3.17), see Appendix E.] As in the Newtonian case, the speed of sound is given by

$$a^2 = \frac{dP}{d\rho} = \frac{dP}{d\rho_0}\frac{d\rho_0}{d\rho} = \frac{dP}{d\rho_0}\frac{\rho_0}{\rho + P} \tag{3.18}$$

[cf. Eq. (ST.G.8)], where we have employed Eq. (3.7) in the last equality. Using Eq. (3.18), we can rewrite dP/dR as

$$\frac{dP}{dR} = \frac{dP}{d\rho_0}\frac{d\rho_0}{dR} = (\rho + P)\, a^2 \frac{{\rho_0}'}{\rho_0}, \tag{3.19}$$

Substituting this expression into (3.17) yields

$$uu' + \frac{M}{R^2} + \left(1 - \frac{2M}{R} + u^2\right) a^2 \frac{{\rho_0}'}{\rho_0} = 0 \tag{3.20}$$

[cf. Eq. (ST.G.9)]. Just as Eq. (3.16) is analogous to Eq. (2.6) in the Newtonian solution, Eq. (3.20) is the relativistic version of the second Newtonian fluid equation (2.8).

3.2 Solution at the critical radius

As in our derivation of the Newtonian equations, we can use the fluid equations (3.16) and (3.20) to solve for u' and ${\rho_0}'$. Combining Eqs. (3.16) and (3.20) to eliminate ρ_0 yields

$$uu' + \frac{M}{R^2} - \left(1 - \frac{2M}{R^2} + u^2\right)\left(\frac{u'}{u} + \frac{2}{R}\right) = 0, \tag{3.21}$$

which can be solved for u' to obtain

$$u' = u\left(\frac{(1 - 2M/R + u^2)\,2a^2/R - M/R^2}{u^2 - (1 - 2M/R + u^2)\,a^2}\right). \tag{3.22}$$

Inserting (3.22) back into (3.16) gives

$$\frac{{\rho_0}'}{\rho_0} = -\frac{(1 - 2M/R + u^2)\,2a^2/R - M/R^2}{u^2 - (1 - 2M/R + u^2)\,a^2} - \frac{2}{R}, \tag{3.23}$$

or

$${\rho_0}' = -\rho_0\left(\frac{2u^2/R - M/R^2}{u^2 - (1 - 2M/R + u^2)\,a^2}\right). \tag{3.24}$$

We can write Eqs. (3.22) and (3.24) more compactly by defining

$$D_1 \equiv \frac{1}{\rho_0}\left[\left(1 - \frac{2M}{R} + u^2\right)\frac{2a^2}{R} - \frac{M}{R^2}\right], \tag{3.25}$$

$$D_2 \equiv \frac{1}{u}\left(\frac{2u^2}{R} - \frac{M}{R^2}\right), \tag{3.26}$$

and

$$D \equiv \frac{1}{\rho_0 u}\left[u^2 - \left(1 - \frac{2M}{R} + u^2\right)a^2\right] \tag{3.27}$$

[cf. Eqs. (ST.G.11), (ST.G.12), and (ST.G.13), respectively]. We then have

$$u' = \frac{D_1}{D}, \qquad {\rho_0}' = -\frac{D_2}{D} \tag{3.28}$$

[cf. Eq. (ST.G.10)]. Note the similarity between Eq. (3.28) and Eq. (2.13) in the Newtonian treatment.

We now demonstrate that for any equation of state obeying $a^2 < 1$ (i.e., for which the speed of sound is less than that of light; this is known as the causality constraint), the flow must pass through a critical point outside the event horizon at $R = 2M$. (Recall that the event horizon is the spherical boundary around the black hole inside which the escape velocity becomes greater than the speed of light.) Evaluating Eq. (3.27) in the limit $R \to \infty$ gives

$$D \simeq \frac{u^2 - a^2}{\rho_0 u} \tag{3.29}$$

[cf. Eq. (ST.G.14)]. Since $u \to 0$ as $R \to \infty$, we must have $D < 0$ at infinity. Evaluating Eq. (3.27) at the horizon, on the other hand, gives

$$D = \frac{u}{\rho_0}\left(1 - a^2\right) \tag{3.30}$$

[cf. Eq. (ST.G.15)], which is necessarily positive. Since D goes from a negative value at infinity to a positive value at the horizon, somewhere in between it must have a value of zero. The radius at which this occurs is called the critical radius, $R = R_s$. To avoid singularities in the flow (i.e., to avoid infinite expressions for u' and ${\rho_0}'$), we must have $D_1 = D_2 = 0$ at $R = R_s$ [cf. Eq. (ST.G.16)].

We can use this fact to solve Eqs. (3.25), (3.26), and (3.27) for u and a at the critical radius. Setting $D_2 = 0$ at $R = R_s$ yields

$$u_s^2 = \frac{M}{2R_s}. \tag{3.31}$$

Similarly, setting $D_1 = 0$ gives

$$\left(1 - \frac{2M}{R_s} + u_s^2\right)\frac{2a^2}{R_s} - \frac{M}{R_s^2} = 0, \tag{3.32}$$

which we can combine with Eq. (3.31) to obtain

$$a_s^2 = \frac{M}{2R_s - 3M}. \tag{3.33}$$

Combining Eqs. (3.31) and (3.33) to eliminate R_s yields

$$u_s^2 = \frac{a_s^2}{1 + 3a_s^2}, \tag{3.34}$$

or

$$a_s^2 = \frac{u_s^2}{1 - 3u_s^2} \tag{3.35}$$

[cf. Eq. (ST.G.17)]. In the Newtonian solution, we found that $u_s = a_s$ at the critical point. It is important to note that in the relativistic solution this is no longer true, as we can see from Eqs. (3.34) and (3.35). One should therefore take the s subscript to refer to the point at which $D_1 = D_2 = D = 0$, not the "transonic" point at which $u = a$.

3.3 Conservation equations

The last major step in our derivation of the relativistic Bondi solution will be to recast equations (3.2) and (3.20) in the form of conservation equations. Just as, in the previous chapter, we used the continuity equation (2.3) to derive Eq. (2.19) for the accretion rate, we can use the law of baryon conservation (3.2) to show that

$$4\pi\rho_0 u R^2 = \text{constant} = \dot{M} \tag{3.36}$$

[cf. Eq. (ST.G.21)]. As before, we find that the accretion rate $\dot{M}$, which we define to be positive for ingoing flow, is independent of the radius R. Eq. (3.20) is slightly more challenging to recast, since it cannot be integrated directly. We start by recognizing that

$$uu' + \frac{M}{R^2} = \frac{1}{2}\left(1 - \frac{2M}{R} + u^2\right)', \tag{3.37}$$

where all primes ($'$) denote total derivatives with respect R. Substituting (3.37) into (3.20) gives

$$\frac{1}{2}\left(1-\frac{2M}{R}+u^2\right)'+\left(1-\frac{2M}{R}+u^2\right)a^2\frac{{\rho_0}'}{\rho_0}=0, \tag{3.38}$$

or

$$\frac{1}{2}\frac{(1-2M/R+u^2)'}{1-2M/R+u^2}+a^2\frac{{\rho_0}'}{\rho_0}=0. \tag{3.39}$$

We would like to be able to rewrite the second term of (3.39) in a similar way (i.e., as the derivative of some expression divided by the expression itself). To this end, we will show that

$$a^2\frac{{\rho_0}'}{\rho_0}=\frac{\rho_0}{\rho+P}\left(\frac{\rho+P}{\rho_0}\right)'. \tag{3.40}$$

Carrying out the total derivative in (3.40) yields

$$\frac{\rho_0}{\rho+P}\left(\frac{\rho+P}{\rho_0}\right)'=\frac{\rho_0}{\rho+P}\left(\frac{\rho'+P'}{\rho_0}-\frac{(\rho+P){\rho_0}'}{\rho_0^2}\right). \tag{3.41}$$

From Eq. (3.7), we have

$$\rho'=\frac{d\rho}{dR}=\frac{d\rho}{d\rho_0}\frac{d\rho_0}{dR}=\frac{\rho+P}{\rho_0}{\rho_0}', \tag{3.42}$$

and from (3.18),

$$P'=\frac{dP}{dR}=\frac{dP}{d\rho_0}\frac{d\rho_0}{dR}=\frac{\rho+P}{\rho_0}a^2{\rho_0}'. \tag{3.43}$$

Inserting (3.42) and (3.43) into (3.41) gives

$$\frac{\rho_0}{\rho+P}\left(\frac{\rho+P}{\rho_0}\right)'=\frac{\rho_0}{\rho+P}\left(\frac{\rho+P}{\rho_0^2}{\rho_0}'+\frac{\rho+P}{\rho_0^2}a^2{\rho_0}'-\frac{\rho+P}{\rho_0^2}{\rho_0}'\right)=a^2\frac{{\rho_0}'}{\rho_0}, \tag{3.44}$$

as desired. Substituting (3.44) into (3.39) then yields

$$\frac{1}{2}\frac{(1-2M/R+u^2)'}{1-2M/R+u^2}+\frac{\rho_0}{\rho+P}\left(\frac{\rho+P}{\rho_0}\right)'=0, \tag{3.45}$$

which can be integrated to obtain

$$\frac{1}{2}\ln\left(1-\frac{2M}{R}+u^2\right)+\ln\left(\frac{\rho+P}{\rho_0}\right)=\text{constant}, \tag{3.46}$$

or

$$\left(\frac{\rho+P}{\rho_0}\right)^2\left(1-\frac{2M}{R}+u^2\right)=\text{constant}=\left(\frac{\rho_\infty+P_\infty}{\rho_{0,\infty}}\right)^2 \tag{3.47}$$

[cf. Eq. (ST.G.22)], where we have determined the constant of integration by evaluating the left side of (3.47) in the limit $R\to\infty$. Eq. (3.47) is known as the relativistic Bernoulli equation, and is the relativistic analogue of Eq. (2.24); the collection of terms on the right-hand side is referred to as the Bernoulli constant.

Finally, we will rewrite the Bernoulli equation (3.47) in terms of the sound speed a. (The resulting equation will prove useful when we go to compute the density profile in the following section.) We begin by combining Eqs. (3.1) and (3.8) to obtain

$$\rho=\rho_0+\frac{P}{\Gamma-1}=\rho_0+\frac{\kappa\rho_0^\Gamma}{\Gamma-1} \tag{3.48}$$

[cf. Eq. (ST.G.25)], where we have employed the polytropic relation (3.14) in the last equality. Using Eqs. (3.14) and (3.48), we can rewrite the first term on the left-hand side of the Bernoulli equation (3.47) as

$$\frac{\rho+P}{\rho_0}=1+\frac{\kappa\rho_0^{\Gamma-1}}{\Gamma-1}+\kappa\rho_0^{\Gamma-1}=1+\frac{\Gamma}{\Gamma-1}\kappa\rho_0^{\Gamma-1} \tag{3.49}$$

[cf. Eq. (ST.G.26)]. Inserting Eqs. (3.14) and (3.49) into Eq. (3.18) for the sound speed a gives

$$a^2=\frac{\Gamma\kappa\rho_0^{\Gamma-1}}{1+\Gamma\kappa\rho_0^{\Gamma-1}/(\Gamma-1)} \tag{3.50}$$

[cf. Eq. (ST.G.27)], or

$$\Gamma\kappa\rho_0^{\Gamma-1}=\frac{a^2}{1-a^2/(\Gamma-1)} \tag{3.51}$$

[cf. Eq. (ST.G.28)]. Combining Eqs. (3.51) into (3.49) yields

$$\frac{\rho+P}{\rho_0}=1+\frac{a^2}{\Gamma-1-a^2}, \tag{3.52}$$

which we can substitute into (3.47) to obtain

$$\left(1+\frac{a^2}{\Gamma-1-a^2}\right)^2\left(1-\frac{2M}{R}+u^2\right)=\left(1+\frac{a_\infty^2}{\Gamma-1-a_\infty^2}\right)^2 \tag{3.53}$$

[cf. Eq. (ST.G.29)].

We have now derived the bulk of the relativistic solution for spherically symmetric, radial accretion onto a black hole. In Appendix B we include a few more notes on the subject (for example, we show how to calculate the accretion rate $\dot{M}$ in terms of the boundary values at infinity, as well as the flow profiles in the limit $R \ll R_s$), but this information is not needed for our main discussion. Finally, note that, as in our treatment of the Newtonian solution, we did not explicitly write down equations for the rest-mass density and velocity as functions of R, since these functions are not known analytically.

3.4 Determining $\rho_0(R)$ and $u(R)$

Now that we have derived the relativistic equations for Bondi accretion onto a black hole, we will show how those equations can be manipulated to obtain radial profiles of the fluid rest-mass density ρ_0 and four-velocity u in Schwarzschild coordinates. (We save calculation of the radial three-velocity and other relevant fluid parameters for Chapter 4.) As mentioned above, it is impossible to obtain an analytical expression for ρ_0 as a function of R. Instead, what we will do here is derive a non-linear equation for ρ_0, which we can then solve numerically at each desired value of R. The velocity profile can be computed straightforwardly once we know $\rho_0(R)$.

The relativistic Bondi solution can be uniquely determined by just four parameters. We choose to specify the adiabatic index Γ, the critical accretion rate $\dot{M}$, the critical radius R_s, and the black hole mass M. (For simplicity, we always take $M = 1$.) It is also possible to calculate the fluid profiles given a different set of initial parameters. For example, one might want to specify the rest-mass density at the critical radius, $\rho_{0,s}$, instead of the accretion rate; as we will see shortly, this choice does not substantially

change the derivation. One could also choose to specify the boundary values at infinity, a_∞ and $\rho_{0,\infty}$, although we will not address this case here.

We begin with our equations for the fluid velocity and the sound speed at the critical radius:

$$u_s^2 = \frac{1}{2}\frac{M}{R_s}, \qquad a_s^2 = \frac{M}{2R_s - 3M} \tag{3.54}$$

[cf. Eqs. (3.31) and (3.33)]. These equations allow us to compute u_s and a_s given the critical radius R_s. We can calculate the rest-mass density at the critical radius, $\rho_{0,s}$, by evaluating the accretion rate equation (3.36) at $R = R_s$:

$$\rho_{0,s} = \frac{\dot{M}}{4\pi R_s^2 u_s}. \tag{3.55}$$

[Note that if we had initially chosen to specify $\rho_{0,s}$ instead of $\dot{M}$, we could use Eq. (3.36) to calculate $\dot{M}$.] We now assume, as we did in our original derivation, that the fluid is a polytrope with equation of state

$$P = \kappa \rho_0^\Gamma, \tag{3.56}$$

where P is the pressure and κ is the polytropic constant. We can calculate κ from a_s by evaluating Eq. (3.51) at $R = R_s$. This yields

$$\kappa = \frac{(\Gamma - 1)\, a_s^2}{\Gamma \rho_s^{\Gamma-1} (\Gamma - 1 - a_s^2)}. \tag{3.57}$$

Since we cannot derive an analytical expression for ρ_0 as a function of R, our goal will be to construct an equation that contains only these two variables, which we can then solve numerically for ρ_0 at each value of R. Consider the relativistic Bernoulli equation in the following form:

$$\left(\frac{\Gamma - 1}{\Gamma - 1 - a^2}\right)^2 \left(1 - \frac{2M}{R} + u^2\right) = \left(\frac{\Gamma - 1}{\Gamma - 1 - a_\infty^2}\right)^2 \tag{3.58}$$

[cf. Eq. (3.53)]. If we evaluate the left-hand side of this equation at $R = R_s$ rather than in the limit $R \to \infty$, we obtain

$$\left(\frac{\Gamma - 1}{\Gamma - 1 - a^2}\right)^2 \left(1 - \frac{2M}{R} + u^2\right) = \left(\frac{\Gamma - 1}{\Gamma - 1 - a_s^2}\right)^2 \left(1 - \frac{2M}{R_s} + u_s^2\right) \equiv E, \tag{3.59}$$

where E is the Bernoulli constant. We now want to express the left-hand side of (3.59) in terms of the rest-mass density ρ_0. From Eqs. (3.49) and (3.52), we have

$$\frac{\Gamma - 1}{\Gamma - 1 - a^2} = 1 + \frac{\Gamma}{\Gamma - 1}\kappa\rho_0^{\Gamma - 1}. \tag{3.60}$$

In addition, we can use the equation for the accretion rate in its more general form,

$$\dot{M} = 4\pi R^2 \rho_0 u \tag{3.61}$$

[cf. Eq. (3.36)], to obtain an expression for u in terms of ρ_0:

$$u = \frac{\dot{M}}{4\pi R^2 \rho_0}. \tag{3.62}$$

Inserting Eqs. (3.60) and (3.62) into (3.59) gives

$$E = \left(1 + \frac{\Gamma}{\Gamma - 1}\kappa\rho_0^{\Gamma - 1}\right)^2 \left[1 - \frac{2M}{R} + \left(\frac{\dot{M}}{4\pi R^2 \rho_0}\right)^2\right]. \tag{3.63}$$

We have thus arrived at an equation that relates ρ_0, the rest-mass density of the fluid, and R, the Schwarzschild radius. We can determine the density profile $\rho_0(R)$ by solving Eq. (3.63) for ρ_0 at each desired value of R using a root-finding algorithm, which is exactly what we do in our numerical code. Once we know ρ_0 at a given R, we can compute the four-velocity $u(R)$ from Eq. (3.62).

In Table 3.1 we list the values of u_s, a_s, $\rho_{0,s}$, κ, and E for the Bondi solution characterized by $\Gamma = 4/3$, $R_s = 10M$, $M = 1$, and an accretion rate of either $\dot{M} = 10^{-5}$, $\dot{M} = 10^{-4}$, or $\dot{M} = 10^{-3}$. As described in Chapter 5, this is the solution that we use in our numerical simulations. Note that u_s and a_s, the velocity and sound speed at the

$\dot{M}$	u_s	a_s	$\rho_{0,s}$	κ	E
10^{-5}	0.2236	0.2425	3.559×10^{-8}	16.29	1.253
10^{-4}	0.2236	0.2425	3.559×10^{-7}	7.560	1.253
10^{-3}	0.2236	0.2425	3.559×10^{-6}	3.509	1.253

Table 3.1 Values of key fluid parameters for the different $\dot{M}$ used in our numerical simulations. We take $\Gamma = 4/3$, $R_s = 10M$, and, for simplicity, $M = 1$.

critical radius, are both independent of $\dot{M}$. Physically, this can be explained by the fact that the Bondi solution neglects the self-gravity of the fluid, i.e., we assume the flow is dominated by the gravitational field of the black hole. Since the Bernoulli constant E is computed directly from u_s and a_s [see Eq. (3.59)], it too should be independent of $\dot{M}$. From Eq. (3.55), we know that, since u_s is constant with respect to $\dot{M}$, the rest-mass density at the critical point $\rho_{0,s}$ should scale with $\dot{M}$. Finally, we know from Eq. (3.57) that $\kappa \propto \rho_{0,s}^{1-\Gamma}$, or, since $\Gamma = 4/3$, $\kappa \propto \rho_{0,s}^{-1/3}$. We note that the value $\Gamma = 4/3$ describes a so-called ultra-relativistic gas, in which the internal energy density is large compared to the proper rest-mass density.

At this point we have all of the tools needed to construct the Bondi solution in Schwarzschild coordinates. We show this solution, with the input parameters listed above, in Fig. 3.1. As in most of our numerical simulations, we use an accretion rate of $\dot{M} = 10^{-4}$. From top to bottom, we plot the rest-mass density ρ_0, the time component of the four-velocity u^t, the radial four velocity u, and the radial three-velocity v. [The latter two quantities can be computed from Eqs. (4.13) and (4.8), respectively.] We note that the Bondi solution in Schwarzschild coordinates (solid lines in Fig. 3.1) does not extend smoothly inside the black hole horizon. In particular, while ρ_0 and u remain continuous across the horizon, u^t diverges, and v, which is computed from u^t, becomes undefined. For this and other reasons (see Chapter 4), Schwarzschild coordinates are unsuitable for numerical simulations, motivating us to transform the original Bondi solution (in Schwarzschild coordinates) into coordinates that are better suited for such purposes. In the following chapter, we transform the Bondi solution into three alternative coordinate systems, namely isotropic coordinates on slices of constant Schwarzschild time (Section

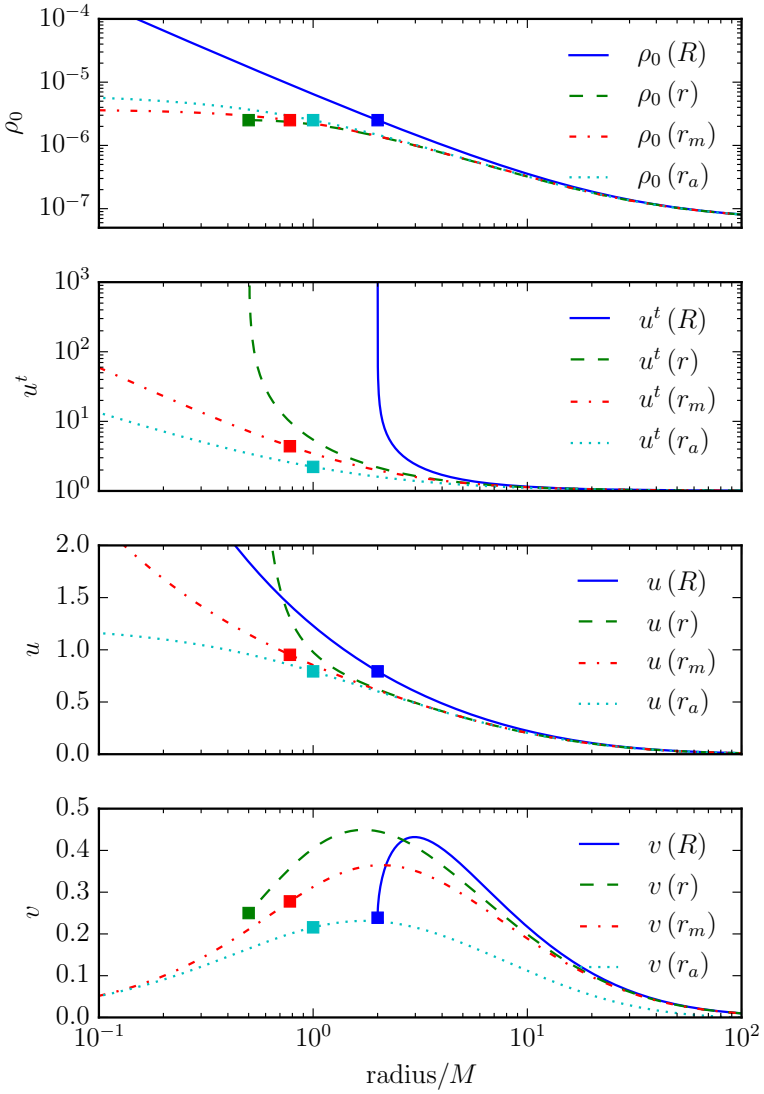

Figure 3.1 Fluid profiles for the Bondi solution described by $\Gamma = 4/3$, $R_s = 10M$, and $\dot{M} = 10^{-4}$ in the four different coordinate systems we discuss in this thesis, namely Schwarzschild coordinates (solid lines), isotropic coordinates on slices of constant Schwarzschild time (dashed lines), maximal trumpet coordinates (dot-dashed lines), and analytical trumpet coordinates (dotted lines). From top to bottom, we show the rest-mass density ρ_0, the time component of the four-velocity u^t, the radial component of the four-velocity $u = -u^r$, and the radial component of the normal three-velocity $v = -v^r$. Boxes mark the location of the horizon in each coordinate system. We note that in both Schwarzschild and isotropic Schwarzschild coordinates $u^t \to \infty$ at the horizon, and, as a result, v becomes undefined. (In isotropic Schwarzschild coordinates $u \to \infty$ at the horizon as well.) In both trumpet coordinate systems, however, all curves penetrate the horizon smoothly. (Compare Fig. 21 in [10].)

4.3), maximal trumpet coordinates (Section 4.4), and analytical trumpet coordinates (Section 4.5). We include, in Fig. 3.1, the equivalent Bondi solution (i.e., using the same input parameters) in each of these coordinate systems alongside our results for Schwarzschild coordinates. We will address these other coordinate systems in more detail later; for now, note that in each of the trumpet coordinate systems the solution is no longer discontinuous at the horizon, and extends smoothly to the coordinate singularity at the origin.

Chapter 4

Coordinate transformations

Now that we have derived the Bondi solution in Schwarzschild coordinates, we will show how we can transform this solution into new isotropic, time-independent coordinate systems. Schwarzschild coordinates, while convenient as an analytical tool, are not well suited for numerical simulations. In general, simulations on a Cartesian grid demand coordinates that are spatially isotropic, i.e., for which the spatial part of the metric can be written as a conformal factor ψ to the fourth power times the flat metric. Moreover, not all isotropic coordinate systems are equally favorable from a numerical relativistic point of view. As we will see below, isotropic coordinates on slices of constant Schwarzschild time, which are one example of an isotropic, time-independent coordinate system, do not support stable evolutions of black hole spacetimes, while coordinate systems with trumpet geometries, two examples of which are described in detail in Sections 4.4 and 4.5, have been shown to be much more effective.

In this chapter, we first introduce some of the basic formalism of the $3+1$ decomposition of Einstein's equations. We then use this formalism to establish a general framework for transforming the original Bondi solution, given in Schwarzschild coordinates, into an arbitrary isotropic, time-independent coordinate system. Finally, we specialize to three different coordinate systems of this type: isotropic coordinates on slices of constant Schwarzschild time, also referred to here as isotropic Schwarzschild coordinates; maximal trumpet coordinates; and analytical trumpet coordinates.

4.1 Introduction to the 3 + 1 decomposition

Einstein's equations of general relativity unite space and time into one fundamental object, *spacetime*, which is represented mathematically by the four-dimensional metric, g_{ab}. However, while this form may be workable for analytical calculations, it is disadvantageous from a numerical point of view. Most numerical codes simulate dynamical systems by first constructing initial data and then evolving those data forward in time. Initial data are obtained by solving so-called constraint equations, while the time evolution is governed by the so-called evolution equations. In order to solve Einstein's equations numerically, we must reformulate them in this way. Such a reformulation requires that we decouple the original equations into their space and time components (the so-called $3 + 1$ decomposition). We end up with one set of equations that constrain the matter and gravitational fields at each instant in time (the constraint equations) and another set that describe how the these objects will evolve (the evolution equations).

Much of the original work in formulating a $3 + 1$ decomposition of Einstein's equations was accomplished by Arnowitt et al. (1962). In the following discussion we employ the ADM equations, which are similar to those developed by Arnowitt et al. and constitute the standard form of the $3 + 1$ decomposition. In our numerical code, however, we implement a different version of the $3 + 1$ decomposition known as the BSSN fomulation [15–17]. We can think about the $3 + 1$ decomposition as a foliation of the four-dimensional spacetime into a stack of three-dimensional, nonintersecting spatial slices of constant coordinate time t. In the ADM formulation of Einstein's equations, the fundamental quantities are the spatial metric γ_{ij} and the extrinsic curvative K_{ij}. Just as the spacetime metric g_{ab} measures distances in four-dimensional spacetime, γ_{ij} measures distances within a (three-dimensional) spatial slice. The extrinsic curvature is related to the first time derivative of the spatial metric and measures the curvature "between" slices.

In the original formulation of Einstein's equations, the line element is given by

$$ds^2 = g_{ab}dx^a dx^b, \tag{4.1}$$

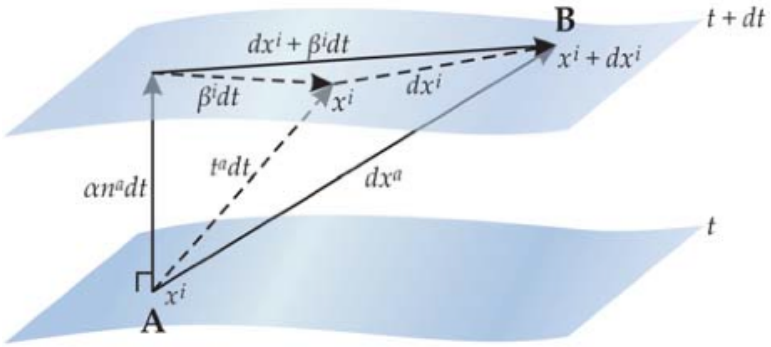

Figure 4.1 Geometry of the $3+1$ decomposition of Einstein's equations. In the $3+1$ decomposition, spacetime, which is four-dimensional, is foliated into three-dimensional spatial slices of constant coordinate time t. Here we show two such slices: one at time t (bottom) and another at time $t+dt$ (top). The displacement vector dx^a goes from point **A**, which exists at time t and has spatial coordinates x^i, to point **B**, which exists at time $t+dt$ and has spatial coordinates x^i+dx^i. As described in the text, the lapse function α measures the advance of proper time between neighboring slices along the normal vector n^a to the original slice, while the shift vector β^i measures the shift in the spatial coordinates from one slice to the next with respect to n^a. (Image from Baumgarte and Shapiro [22].)

where g_{ab} is the four-dimensional (spacetime) metric. In the $3+1$ decomposition, the line element is rewritten as

$$ds^2 = -\alpha^2 dt^2 + \gamma_{ij}\left(dx^i + \beta^i dt\right)\left(dx^j + \beta^j dt\right), \tag{4.2}$$

where α is called the lapse function, β^i is the shift vector, and γ_{ij} is the spatial metric. We note that for spatially isotropic coordinates (e.g., the three coordinate systems we will consider here), we can write the spatial metric as $\gamma_{ij} = \psi^4 \eta_{ij}$, where ψ is known as the conformal factor and $\eta_{ij} = \mathrm{diag}\left(1, r^2, r^2 \sin^2\theta\right)$ is the flat metric. The lapse function α describes how much proper time elapses between neighboring spatial slices as measured along the normal vector to each slice, denoted n^a. It can be shown (see, e.g., Chapter 2 of [22]) that

$$n^a = \left(\alpha^{-1}, -\alpha^{-1}\beta^i\right), \tag{4.3}$$

or

$$n_a = (-\alpha, 0, 0, 0). \tag{4.4}$$

The shift vector β^i measures how much spatial coordinates "shift" from one slice to the next with respect to the normal vector. (See Fig. 4.1 for an illustration of the geometry of the 3+1 decomposition.) Together, the lapse and shift completely embody the coordinate freedom inherent in general relativity, and can therefore be chosen arbitrarily. As we will note again in Chapter 5, it is often the case that a particular choice of the lapse and shift is more useful for numerical applications.

4.2 General expressions

Now that we have introduced some of the formalism of the $3 + 1$ decomposition, we can develop a general framework for transforming the Bondi solution into an arbitrary time-independent, isotropic coordinate system.

Any coordinate system that describes the Schwarzschild spacetime can be derived from the metric in Schwarzschild coordinates by employing a series of coordinate transformations. In each of the coordinate systems considered here, the angular coordinates remain unchanged; therefore, starting from the Schwarzschild solution in Schwarzschild coordinates, we can arrive at each of these coordinate systems in at most two steps: a transformation of the time coordinate and a transformation of the radial coordinate. Likewise, we can transform the Bondi solution, which is given in Schwarzschild coordinates, into an arbitrary coordinate system by performing the corresponding coordinate transformations.

We first transform to a new time coordinate t, which allows for a different slicing of the Schwarzschild spacetime, while keeping as our radial coordinate the Schwarzschild radius R (see Fig. 4.2). Under this transformation, t is related to the Schwarzschild time T by

$$t = T + h\left(R\right), \tag{4.5}$$

where $h\left(R\right)$ is a so-called height function that depends on the radial coordinate only (see, e.g., Chapter 4 of [22] for a detailed discussion). Since (4.5) is a transformation of the time coordinate only, and since all of the fluid variables are time-independent (i.e., since we are considering steady-state solutions), all covariant spatial components of tensors, as

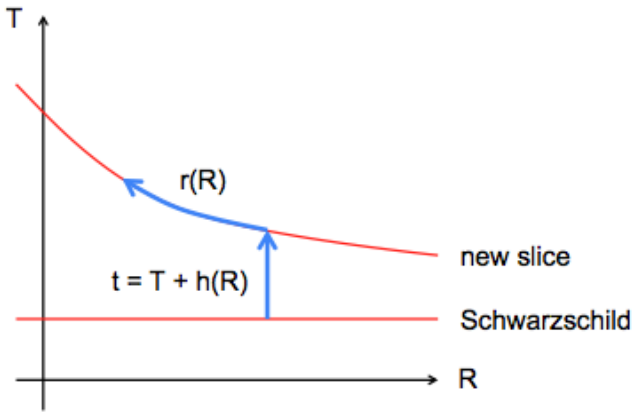

Figure 4.2 Transformation from Schwarzschild coordinates to an arbitrary time-independent coordinate system. As described in the text, we perform this transformation in two steps. First, we transform from the Schwarzschild time T to a new time coordinate t by introducing a so-called height function $h\,(R)$ (vertical arrow). We then transform to a new isotropic radial coordinate r within the resulting spatial slice (curved arrow).

well as all scalars, remain unchanged. It can also be shown (see Appendix F) that the form of the fluid equations (3.16) and (3.17) is invariant under this transformation.

In the second step, we transform from the Schwarzschild radius R to a new isotropic radial coordinate r within each new spatial slice. We note that R is also referred to as an "areal" radius because the proper area of a sphere of radius R in the Schwarzschild spacetime is $4\pi R^2$, as in flat space; R is therefore related to a physically measurable quantity, and, unlike the other (isotropic) radial coordinates that we will encounter in this chapter, has an invariant meaning.

We now consider how the fluid variables ρ_0 and u^r behave under these transformations. As the time component of the density four-vector, the rest-mass density is invariant under spatial transformations. Alternatively, since the fluid equations are invariant under time transformations of the form (4.5), and the rest-mass density is computed directly from these equations (see Section 3.4), it must also be invariant under the time transformation. In practice, this means that if ρ_0 takes some value at a certain areal radius R in Schwarzschild coordinates, it will take the same value at the corresponding isotropic radius r.

We can compute u^r from the general formula for transformation of four-vectors. If $\mathbf{A}$ is an arbitrary four-vector in some coordinate system S, then the components of $\mathbf{A}'$, the

corresponding vector in a different coordinate system, are given by the transformation

$$A^{a'} = \frac{\partial x^{a'}}{\partial x^b} A^b, \tag{4.6}$$

where the summation is over all of the coordinates in S, denoted x^b. Using this rule, we find that u^r, the radial four-velocity in the new coordinate system, is given by

$$u^r = \frac{\partial r}{\partial x^b} u^b = \frac{\partial r}{\partial t} u^t + \frac{\partial r}{\partial R} u^R + \frac{\partial r}{\partial \theta} u^\theta + \frac{\partial r}{\partial \phi} u^\phi = \frac{\partial r}{\partial R} u^R, \tag{4.7}$$

where the last equality is true because we are assuming r depends on R only (and $u^\theta = u^\phi = 0$). Here u^R is the radial four-velocity in Schwarzschild coordinates, which can be computed as outlined in Section 3.4.

We would also like to compute three-velocity of the fluid as measured by a normal observer,

$$v^a \equiv \frac{1}{W} \gamma^a{}_b u^b = \left(0, \frac{u^i}{W} + \frac{\beta^i}{\alpha} \right) \tag{4.8}$$

[cf. Eq. (27) in [25]], which is used in many formulations of relativistic hydrodynamics. Here W is the Lorentz factor between a normal observer and an observer comoving with the fluid, defined as

$$W \equiv -n_a u^a = \alpha u^t \tag{4.9}$$

[cf. Eq. (26) in [25]], where n_a is the covariant form of the normal vector (4.4). Note that, since we are assuming radial flow, the only nonzero component of v^i will be the radial component.

We recognize that, in order to compute v^r, we need to know the time component of the fluid four-velocity, u^t, in addition to the radial component (4.7). One way to compute u^t would be to start from the expression in Schwarzschild coordinates [Eq. (E.21)] and perform the transformations described above. Alternatively, since the flow is purely radial, we can compute u^t from the normalization of the four-velocity,

$$u_a u^a = -1. \tag{4.10}$$

We begin by noting that for spherically symmetric coordinate systems, the shift will be zero except in the radial direction: $\beta^i = (\beta, 0, 0)$. As a result, we can rewrite the metric (4.2) as

$$ds^2 = \left(-\alpha^2 + \psi^4\beta^2\right) dt^2 + 2\psi^4\beta dt dr + \psi^4 \left(dr^2 + r^2 d\Omega^2\right). \tag{4.11}$$

Using this metric, the normalization condition (4.10) gives

$$\begin{aligned} -1 = g_{ab}u^a u^b &= g_{tt}\left(u^t\right)^2 + 2g_{tr}u^t u^r + g_{rr}\left(u^r\right)^2 \\ &= \left(-\alpha^2 + \psi^4\beta^2\right)\left(u^t\right)^2 + 2\psi^4\beta u^t u^r + \psi^4\left(u^r\right)^2, \end{aligned} \tag{4.12}$$

or, substituting $u = -u^r$ and solving for u^t using the quadratic formula,

$$u^t = \frac{1}{\alpha^2 - \psi^4\beta^2}\left[-\psi^4\beta u + \sqrt{\psi^8\beta^2u^2 + \left(\alpha^2 - \psi^4\beta^2\right)\left(\psi^4u^2 + 1\right)}\right]. \tag{4.13}$$

For $\beta^i = 0$, the above expression simplifies to

$$u^t = \alpha^{-1}\sqrt{\psi^4u^2 + 1}. \tag{4.14}$$

We have now developed all of the machinery necessary to transform the Bondi solution in Schwarzschild coordinates into an arbitrary time-independent, isotropic coordinate system. Our method can be summarized as follows. We first compute the fluid variables ρ_0 and u^R in Schwarzschild coordinates as outlined in Section (3.4), but express the radial dependence in terms of r rather than R. We then transform the radial four-velocity u^R using Eq. (4.7) and compute u^t from Eq. (4.13). Finally, we compute v^r by inserting these quantities into Eq. (4.8). In Table 4.1 we summarize the key results for each of the coordinate systems discussed below, along with the equivalent expressions in Schwarzschild coordinates.

	Schwarzschild	Isotropic	Maximal trumpet	Analytical trumpet
α	$\left(1-\frac{2M}{R}\right)^{1/2}$	$\frac{1-M/2r}{1+M/2r}$	f	$\frac{r}{r+M}$
β^r	0	0	$\frac{C}{\psi^2 R^2}$	$\frac{Mr}{(r+M)^2}$
ψ	N/A	$1+\frac{M}{2r}$	$\left(\frac{R}{r}\right)^{1/2}$	$\left(1+\frac{M}{r}\right)^{1/2}$
K	0	0	0	$\frac{M}{(r+M)^2}$
r_h	$2M$	$M/2$	$0.779M$	M
u^r	u^R	$\frac{u^R}{(1+M/2r)(1-M/2r)}$	$\frac{u^R}{\psi^2 f}$	u^R

Table 4.1 Expressions for the lapse α, the radial component of the shift β^r, the conformal factor ψ, the mean curvature K, the location of the horizon r_h, and the radial component of the four-velocity u^r for each of the coordinate systems considered below. (The column labeled "isotropic" refers to isotropic coordinates on slices of constant Schwarzschild time.) As in the text, we express the radial four-velocity in terms of u^R, the velocity in Schwarzschild coordinates. Regarding maximal trumpet coordinates, the quantities f, r, and ψ are given by Eqs. (4.32), (4.37), and (4.38), respectively; while the expressions listed in the table appear to be fairly concise, they are actually quite complicated, as the referenced equations reveal. Regarding analytical trumpet coordinates, we show expressions for the special case $R_0 = M$ that we ultimately use in our numerical simulations (see Section 4.5). Finally, we note that since Schwarzschild coordinates, in which the line element is given by (3.15), are not isotropic, we cannot express the spatial metric as a conformal factor ψ times the flat metric, i.e., the conformal factor is undefined.

4.3 Isotropic Schwarzschild coordinates

4.3.1 Overview

We will now use the general prescription outlined in the previous section to transform the Bondi solution into *isotropic coordinates on slices of constant Schwarzschild time*. In these coordinates, the metric takes the form

$$ds^2 = -\left(\frac{1-M/2r}{1+M/2r}\right)^2 dt^2 + \left(1+\frac{M}{2r}\right)^4 \left(dr^2 + r^2 d\Omega^2\right), \tag{4.15}$$

where M is the mass of the black hole, t is the Schwarzschild time, and r is the isotropic radius, which is related to the Schwarzschild radius R by

$$R = r\left(1 + \frac{M}{2r}\right)^2. \tag{4.16}$$

The inverse radial transformation is

$$r = \frac{R - M \pm \sqrt{R\,(R - 2M)}}{2}, \tag{4.17}$$

and is double-valued. Comparing (4.15) with the general metric in $3+1$ form (4.2) yields the lapse,

$$\alpha = \frac{1 - M/2r}{1 + M/2r}, \tag{4.18}$$

the shift,

$$\beta^i = 0, \tag{4.19}$$

and the spatial metric $\gamma_{ij} = \psi^4 \eta_{ij}$, where

$$\psi = 1 + \frac{M}{2r}. \tag{4.20}$$

We also find it useful to compute the extrinsic curvature K_{ij}, which, as mentioned in Section 4.1, describes the curvature between spatial slices, and the mean curvature $K \equiv \gamma^{ij} K_{ij}$. We can calculate K_{ij} from

$$K_{ij} = \frac{1}{2\alpha}\left(-\partial_t \gamma_{ij} + D_i \beta_j + D_j \beta_i\right), \tag{4.21}$$

where D_i is the covariant derivative associated with the spatial metric, γ_{ij}. For isotropic Schwarzschild coordinates, $\partial_t \gamma_{ij}$ and β^i both vanish, so we have

$$K_{ij} = 0 \tag{4.22}$$

and

$$K \equiv \gamma^{ij} K_{ij} = 0. \tag{4.23}$$

In isotropic Schwarzschild coordinates, the black hole horizon is located at $r = M/2$. [One can show this by inserting $R = 2M$ into Eq. (4.17) for the isotropic radius.] From Eq. (4.18), we see that the lapse vanishes at this point, which means that the coordinates do not penetrate the horizon, and instead cover only the region of the Schwarzschild spacetime corresponding to $R > 2M$. To make sense of this, recall that from above that the isotropic radius r is actually double-valued, i.e., every areal radius $R > 2M$ corresponds to two values of r. Physically, this means that the coordinates (4.15) describe two copies of the exterior of the black hole, with $r = 0$ on one copy corresponding to spatial infinity on the other. The black hole horizon at $r = M/2$ marks the division between the two spacetimes, sometimes referred to as the "throat" of the black hole. (See, e.g., Chapter 3 of [22] for a more detailed discussion.)

From a numerical relativistic point of view, the fact that isotropic Schwarzschild coordinates do not extend inside the horizon (and become singular at the horizon) poses a significant problem. Most notably, it means that it is not possible to perform stable numerical simulations of black hole spacetimes in these coordinates. In addition, if we imagined simulating accretion onto a black hole expressed in isotropic Schwarzschild coordinates, the inflowing matter would simply accumulate at the horizon. As we will describe in more detail in Section 4.4, one method that has been developed to circumvent this issue is to cast the black hole initial data in isotropic Schwarzschild coordinates and then evolve it with certain coordinate conditions [e.g., Eqs. (5.2) and (5.3)] that force the solution to settle down to a steady state that can be handled numerically.

4.3.2 Transformation of the Bondi solution

With this in mind, we now consider the Bondi solution under the transformation to isotropic Schwarzschild coordinates. As discussed in Section 4.2, the rest-mass density ρ_0 remains invariant under such a transformation; thus, it can be calculated as described in Section 3.4. From Eq. (4.7), we find that the radial component of the fluid four-velocity

can be expressed as

$$\begin{aligned} u^r &= \frac{\partial r}{\partial R} u^R = \left(\frac{\partial R}{\partial r}\right)^{-1} u^R \\ &= u^R \left[\frac{\partial}{\partial r}\left(r\left(1+\frac{M}{2r}\right)^2\right)\right]^{-1} \\ &= \frac{u^R}{(1+M/2r)\,(1-M/2r)} \end{aligned} \tag{4.24}$$

[cf. Eq. (B14) in [10]]. Inserting our expressions for the lapse [Eq. (4.18)] and conformal factor [Eqs. (4.20)] into (4.14) gives, for the time component of the four-velocity,

$$u^t = \frac{1+M/2r}{1-M/2r}\left[\left(1+\frac{M}{2r}\right)^4 u^2 + 1\right]^{1/2}. \tag{4.25}$$

(Note that $u = -u^r$, i.e., the inward velocity after transforming to isotropic coordinates.) Since u^t is the time component of the velocity four-vector, it is invariant under the (spatial) transformation from Schwarzschild to isotropic Schwarzschild coordinates. Consequently, we could derive the same result by simply rewriting our expression for u^t in Schwarzschild coordinates [Eq. (E.21)] in terms of r instead of R. Finally, we can insert (4.24) and (4.25) into (4.8) to compute the new radial three-velocity of the fluid,

$$v^r = -u\left[\left(1+\frac{M}{2r}\right)^4 u^2 + 1\right]^{1/2}, \tag{4.26}$$

thereby completing the transformation of the Bondi solution into isotropic Schwarzschild coordinates.

Eqs. (4.24), (4.25), and (4.26) for u^r, u^t, and v^r, respectively, are plotted in Fig. 3.1, along with the rest-mass density ρ_0. As shown in the figure, both u^t and u^r diverge at the horizon. In addition, all other quantities become undefined at that point due to the coordinate singularity. Consequently, we cannot use isotropic Schwarzschild coordinates in their natural form to construct initial data for our numerical simulations. To get around this issue, we modify the analytical solution in the vicinity of the black hole ($r < M$) by introducing artificial initial data that are finite (if not well-behaved) all

the way to $r = 0$. While not a particularly elegant solution, this method has been used (see, e.g., [10]) to generate stable simulations of Bondi accretion in black hole spacetimes. We describe our method of constructing artificial initial data in isotropic Schwarzschild coordinates in Section 5.2. In the following section, we describe what we believe is a much more powerful alternative to this approach that involves casting the Bondi initial data in so-called "trumpet" coordinates. In addition to their other advantages, described below, these coordinates do not require modification of the initial data in the vicinity of the horizon.

4.4 Maximal trumpets

We will now perform the same set of calculations for a different coordinate system, namely a *maximally sliced trumpet*. However, before we discuss this particular coordinate system in detail, we will briefly introduce so-called "trumpet" geometries, and explain why they have proven to be extremely useful in the context of numerical relativity.

Two of the primary issues that arise in simulations of black hole spacetimes are the treatment of the central singularity and the treatment of the event horizon. In the previous section, we discussed isotropic coordinates on slices of constant Schwarzschild time, which avoid the first issue by covering only the exterior of the black hole. However, they still have the problem of a coordinate singularity at the horizon, and for this reason do not allow for stable evolutions of black holes or black hole accretion.

In order to address both of these issues, many recent numerical codes (e.g., [13, 14]) have used so-called moving-puncture coordinates, which consist of a "1 + log" slicing condition for the lapse [18] and a Gamma-driver condition for the shift vector [19]. [See Eqs. (5.2) and (5.3), respectively, for a mathematical description of these conditions.] Over the course of the evolution, these two conditions act to bring the black hole, which is initially described in isotropic Schwarzschild coordinates, into a trumpet geometry (see, e.g., [20, 21] for a detailed discussion). In contrast to many other coordinate systems, including isotropic Schwarzschild coordinates, the resulting trumpet coordinates penetrate the black hole horizon smoothly and terminate on a sphere of nonzero (finite)

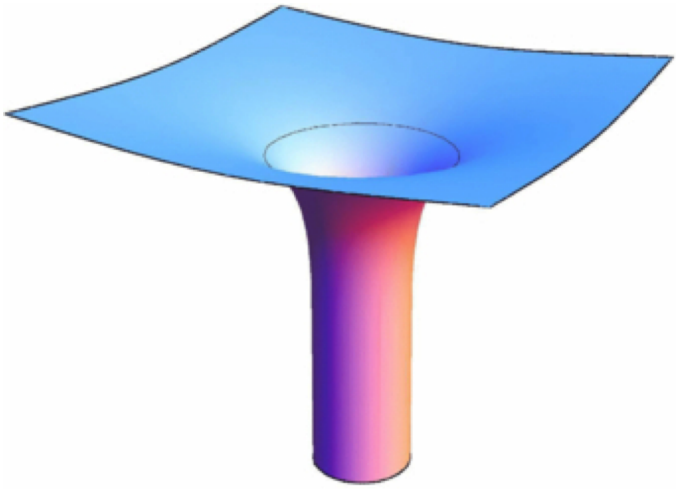

Figure 4.3 Embedding diagram for the analytical trumpet coordinate system (Section 4.5) characterized by $R_0 = M$. Here the areal radius R of a point on the slice is given by the distance from the axis of symmetry. The circle at the top of the figure marks the event horizon at $R = 2M$. As is typical of trumpet coordinate systems, the slice has an asymptotically cylindrical end inside the horizon and an asymptotically flat end at infinity. (Image from Dennison and Baumgarte [23].)

areal radius, thereby avoiding numerical issues associated with the central singularity. Furthermore, any point on this so-called "limiting surface" is an infinite proper distance away from all other points on the same spatial slice. Spatial slices in trumpet coordinates asymptote to a cylinder inside the black hole horizon and become asymptotically flat in the limit $r \to \infty$ (see Fig. 4.3).

In this and following section we will introduce the two examples of trumpet coordinate systems that we use in our numerical simulations. Maximally sliced trumpets, which we discuss in this section, can be understood semi-analytically [26], while analytical trumpets, discussed in Section 4.5, are fully analytical [23]. Once we have established the basic geometry of each coordinate system, we will follow the prescription outlined in Section 4.2 and show how the Bondi solution can be transformed into the new coordinates.

4.4.1 Overview

In Section 4.1 we noted that the coordinate freedom of general relativity enables us to impose certain coordinate conditions that constrain the behavior of our solution. For example, we might want to specify expressions for the lapse and shift. One such condition that is particularly useful from a numerical point of view is the so-called maximal slicing condition,

$$K = 0, \tag{4.27}$$

where $K \equiv \gamma^{ij} K_{ij}$ is the mean curvature. Isotropic coordinates on slices of constant Schwarzschild time are one example of a maximal slicing of the Schwarzschild spacetime. In fact, it is possible to derive a whole family of maximally sliced coordinate systems from the Schwarzschild metric by introducing a time transformation

$$t = T + h\left(R\right). \tag{4.28}$$

Note that this transformation is of the same form as the one we considered in Section 4.2 [Eq. (4.5)]. The resulting family of coordinate systems is time-independent, and is described by the spatial metric

$$\gamma_{ij} dx^i dx^j = f^{-2} dR^2 + R^2 d\Omega^2, \tag{4.29}$$

the lapse,

$$\alpha = f, \tag{4.30}$$

and the shift,

$$\beta^R = \frac{Cf}{R^2} \tag{4.31}$$

[cf. Eqs. (3a), (3b), and (3c) in [26]]. The function f is given by

$$f = \left(1 - \frac{2M}{R} + \frac{C^2}{R^4}\right)^{1/2} \tag{4.32}$$

[cf. Eq. (3d) in [26]], where C is an arbitrary parameter. Note that for $C = 0$ we recover the original Schwarzschild solution. It was demonstrated by [27] that the slicing condition

$$\partial_t \alpha = -2\alpha K, \tag{4.33}$$

a version of the "$1 + \log$" slicing described above, causes numerical simulations of black holes to settle down into a member of this family of coordinate systems with $C = 3\sqrt{3}M^2/4$; this value of C corresponds to a maximal trumpet geometry with a limiting surface of areal radius $R = 3M/2$.

In order to use this solution to construct initial data for our numerical code, it is necessary to transform it into isotropic coordinates. As shown in [26], this can be done analytically. We start by equating the spatial metric (4.29) with its counterpart in isotropic form:

$$f^{-2}dR^2 + R^2 d\Omega^2 = \psi^4 \left(dr^2 + r^2 d\Omega^2\right) \tag{4.34}$$

[cf. Eq. (4) in [26]]. We then have

$$R^2 = \psi^4 r^2 \tag{4.35}$$

and

$$f^{-2}dR^2 = \psi^4 dr^2 \tag{4.36}$$

[cf. Eqs. (5) and (6) in [26], respectively]. Combining Eqs. (4.35) and (4.36) and integrating yields an expression for r in terms of the areal radius R:

$$\begin{aligned} r = &\left[\frac{2R + M + \left(4R^2 + 4MR + 3M^2\right)^{1/2}}{4}\right] \\ &\times \left[\frac{\left(4 + 3\sqrt{2}\right)(2R - 3M)}{8R + 6M + 3\left(8R^2 + 8MR + 6M^2\right)^{1/2}}\right]^{1/\sqrt{2}} \end{aligned} \tag{4.37}$$

[cf. Eq. (11) in [26]]. Note that this r is different from the r in isotropic Schwarzschild coordinates. In these coordinates, the black hole horizon is located at $r \simeq 0.799M$. As expected, we have $R \to 3M/2$ as $r \to 0$. Combining Eqs. (4.35) and (4.37) yields the conformal factor

$$\begin{aligned} \psi = &\left[\frac{4R}{2R + M + \left(4R^2 + 4MR + 3M^2\right)^{1/2}}\right]^{1/2} \\ &\times \left[\frac{8R + 6M + 3\left(8R^2 + 8MR + 6M^2\right)^{1/2}}{\left(4 + 3\sqrt{2}\right)(2R - 3M)}\right]^{1/2\sqrt{2}} \end{aligned}, \tag{4.38}$$

[cf. Eq. (12) in [26]]. We note that ψ diverges at $r = 0$ ($R = 3M/2$), indicating that this point represents a coordinate singularity. We can expand (4.38) to find $\psi \approx (3M/2r)^{1/2}$ in the limit $r \to 0$ [cf. Eq. (13) in [26]]. The proper length along a radial segment is then $ds = \psi^2 dr = (3M/2r)\, dr$, which diverges logarithmically at $r = 0$. We therefore

have a limiting surface at $r = 0$ that is an infinite proper distance from the rest of the spatial slice. We refer to the coordinate singularity at $r = 0$ as a "puncture" (as in "moving-puncture" coordinates). In isotropic coordinates, the lapse is given by

$$\alpha = \left(1 - \frac{2M}{R} + \frac{27M^4}{16R^4}\right)^{1/2} \tag{4.39}$$

and the shift by

$$\beta^r = \frac{dr}{dR}\beta^R = \frac{3\sqrt{3}M^2}{4}\frac{r}{R^3} = \frac{3\sqrt{3}M^2}{4}\frac{1}{\psi^2 R^2} \tag{4.40}$$

[cf. Eqs. (14), and (15) in [26], respectively].

As for isotropic Schwarzschild coordinates, we compute the extrinsic curvature K_{ij} from Eq. (4.21). We find that the nonzero components of K_{ij} are

$$K_{rr} = -\frac{2\psi^4 C}{R^3}, \qquad K_{\theta\theta} = \frac{K_{\phi\phi}}{\sin^2\theta} = \frac{C}{R}. \tag{4.41}$$

(For detailed calculations of these expressions, see Appendix G). A quick check, also included in Appendix G, confirms that the trace of the mean curvature vanishes ($K = 0$), as expected.

4.4.2 Transformation of the Bondi solution

As discussed in Section 4.2, the rest-mass density ρ_0 is invariant under the transformation from Schwarzschild to maximal trumpet coordinates and can therefore be computed as outlined in Section 3.4. We compute the radial four-velocity of the fluid from Eq. (4.7), which yields

$$u^r = \frac{dr}{dR}u^R = \frac{u^R}{\psi^2 f}. \tag{4.42}$$

Here u^R is the four-velocity as expressed in Schwarzschild coordinates and ψ and f are given by Eqs. (4.38) and (4.32), respectively. We have used Eq. (4.36) to evaluate the derivative of r with respect to R. As above, the time component of the four-velocity can

be computed from Eq. (4.13), giving

$$u^t = \frac{1}{R-2M}\left[-\frac{C\psi^2}{R}u + \left(\frac{C^2\psi^4}{R^2}u^2 + R\left(R-2M\right)\left(\psi^4u^2+1\right)\right)^{1/2}\right]$$
$$= \frac{1}{\psi^2 r-2M}\left[-\frac{C}{r}u + \left(\frac{C^2}{r^2}u^2 + \psi^2 r\left(\psi^2 r-2M\right)\left(\psi^4u^2+1\right)\right)^{1/2}\right], \qquad (4.43)$$

where $C = 3\sqrt{3}M^2/4$ and we have substituted $u = -u^r$. Before moving on, we note a potential problem with Eq. (4.43), namely that both the numerator and denominator go to zero as we approach the horizon ($R \to 2M$). We know (see Fig. 3.1) that u^t remains finite across the horizon and diverges only at the coordinate singularity at $r = 0$ ($R = 3M/2$). However, in order to compute u^t at the horizon, we need to rewrite Eq. (4.43) to get rid of singular terms. We can accomplish this using a Taylor expansion. First, we rewrite Eq. (4.43) as

$$u^t = \frac{1}{R-2M}\frac{C\psi^2}{R}u\left[-1 + \left(1 + \frac{R^3}{C^2\psi^4}\frac{1}{u^2}\left(R-2M\right)\left(\psi^4u^2+1\right)\right)^{1/2}\right]. \qquad (4.44)$$

We now expand in a Taylor series about $R = 2M$, keeping only the first two non-vanishing terms. We see that the leading-order terms cancel, and we are left with

$$u^t \approx \frac{R^2}{2C\psi^2}\frac{1}{u}\left(\psi^4u^2+1\right) = \frac{\psi^2r^2}{2C}\frac{1}{u}\left(\psi^4u^2+1\right), \qquad (4.45)$$

where all terms on the right-hand side are evaluated at the horizon. Note that it is somewhat arbitrary whether we express these quantities in terms of areal or isotropic radius, since in the case of maximal trumpet coordinates the conformal factor is given in terms of R [see Eq. (4.38)], and the equation for r [Eq. (4.37)] cannot be inverted to find R as a function of r. In our numerical code, we use r whenever possible, and convert to R if needed; here, for completeness, we present both expressions. Finally, the normal three-velocity of the fluid v^r can be computed from Eq. (4.8). We do not include the result here, since it is fairly complicated and we only use the general expression (4.8) in our numerical code.

Plots of ρ_0, u^t, u^r, and v^r for maximal trumpet coordinates are included in Fig. 3.1. Unlike in isotropic Schwarzschild coordinates, all of these quantities remain finite and well-behaved inside the black hole horizon. From a numerical point of view, this means that we no longer have to introduce artificial initial data in the vicinity of the black hole.

4.5 Analytical trumpets

4.5.1 Overview

We now turn our attention to the second example of a trumpet coordinate system that we will use in our numerical code, namely the *analytical trumpet* of [23]. We begin by noting that when we refer to analytical trumpets, we are actually referring to a family of isotropic, trumpet-like coordinate systems. We will ultimately choose one (particularly simple) member of this family to use in our numerical simulations, but for now we will keep our discussion completely general.

In analytical trumpet coordinates, the four-dimensional metric is given by

$$ds^2 = -\frac{r + R_0 - 2M}{r + R_0} dt^2 + \frac{2 f_1}{r} dt dr + \left(1 + \frac{R_0}{r}\right)^2 \left(dr^2 + r^2 d\Omega^2\right) \tag{4.46}$$

[cf. Eq. (1) in [23]], where r is the isotropic radius and R_0 is a constant that parameterizes each member of the family. We have also defined, for convenience,

$$f_1(r) \equiv \sqrt{2r(M - R_0) + R_0(2M - R_0)} \tag{4.47}$$

[cf. Eq. (2) in [23]]. As shown in [23], the line element (4.46) can be derived from the line element for Schwarzschild coordinates by introducing a time transformation

$$t = T + h(R), \tag{4.48}$$

where T is the Schwarzschild time, followed by a radial transformation to an isotropic radial coordinate

$$r = R - R_0, \tag{4.49}$$

where $0 \leq R_0 \leq M$. Note that the time transformation (4.48) is of the same form as the one considered in the context of maximal trumpet coordinates [Eq. (4.28)], although, since we are no longer considering maximal slicing, the height function $h(R)$ takes a different form. We note from the relation between r and R that $r = 0$ corresponds to a nonzero areal radius $R = R_0$. In other words, the coordinates terminate on a sphere of areal radius R_0.

By comparing (4.46) with the general metric in $3+1$ form (4.2), we can identify the lapse,

$$\alpha = \frac{r}{r + R_0}, \tag{4.50}$$

the radial component of the shift vector,

$$\beta^r = \frac{r f_1}{(r + R_0)^2}, \tag{4.51}$$

and the spatial metric $\gamma_{ij} = \psi^4 \eta_{ij}$, where

$$\psi = \left(1 + \frac{R_0}{r}\right)^{1/2} \tag{4.52}$$

[cf. Eqs. (13) and (15) in [23]]. We note that, as in maximal trumpet coordinates, ψ has a $1/r$ dependence, which means that the proper length of a radial segment, given by $ds = \psi^2 dr = (1 + R_0/r)\, dr$, diverges logarithmically at the puncture ($r = 0$). We therefore conclude that any point on the limiting surface at $r = 0$ is an infinite proper distance away from the rest of the spatial slice. The nonzero components of the extrinsic curvature, computed using Eq. (4.21), are

$$K_{rr} = -\frac{r\,(M - R_0) + M R_0}{f_1 r^2}, \qquad K_{\theta\theta} = \frac{K_{\phi\phi}}{\sin^2\theta} = f_1 \tag{4.53}$$

[cf. Eq. (16) in [23]], and the mean curvature is

$$K \equiv \gamma^{ij} K_{ij} = \frac{(3r + 2R_0)(M - R_0) + MR_0}{f_1 (r + R_0)^2}. \tag{4.54}$$

[cf. Eq. (17) in [23]]. (Once again, complete derivations of these results can be found in Appendix G.) In our simulations of Bondi flow in analytical trumpet coordinates, we specialize to the case $R_0 = M$, for which many of the above expressions simplify significantly.

4.5.2 Transformation of the Bondi solution

We will now use the prescription given in Section 4.2 to determine how the fluid variables change under the transformation to analytical trumpet coordinates. First, we note that the rest-mass density once again remains invariant under this transformation, and be computed as described in Section 3.4. As above, the radial four-velocity of the fluid can be computed from Eq. (4.7), which gives the remarkably simple result

$$u^r = \frac{dr}{dR} u^R = u^R. \tag{4.55}$$

We calculate the time-component of the four-velocity from Eq. (4.13), which yields

$$u^t = \frac{r + R_0}{r + R_0 - 2M} \left[-\frac{f_1}{r} u + \left(\frac{r + R_0 - 2M}{r + R_0} + u^2 \right)^{1/2} \right], \tag{4.56}$$

where f_1 is given by Eq. (4.47). (Note that here, as above, we have used $u = -u^r$.) If we consider Eq. (4.56) more carefully, we recognize that, as in the case of maximal trumpet coordinates, we encounter a problem at the black hole horizon, $R = 2M$. In analytical trumpet coordinates, the horizon occurs at an isotropic radius $r = 2M - R_0$ [see Eq. (4.49)]. However, if we insert $r = 2M - R_0$ into our expression for f_1 [Eq. (4.47)], we get $f_1 = 2M - R_0$, so f_1 and r are equal at the horizon. As a result, both the numerator and denominator of (4.56) go to zero as $R \to 2M$, and we need to use a Taylor expansion to evaluate u^t in this limit. We first recognize that we can rewrite

$(r + R_0 - 2M) / (r + R_0)$ as $(r^2 - f_1^2) / (r + R_0)^2$. Our expression for u^t then becomes

$$u^t = \frac{(r + R_0)^2}{r^2 - f_1^2} \left[-\frac{f_1}{r} u + \left(\frac{r^2 - f_1^2}{(r + R_0)^2} + u^2 \right)^{1/2} \right], \tag{4.57}$$

which we rewrite as

$$u^t = \frac{(r + R_0)^2}{r^2 - f_1^2} \left[-\frac{f_1}{r} u + u \left(\frac{r^2 - f_1^2}{(r + R_0)^2} \frac{1}{u^2} + 1 \right)^{1/2} \right]. \tag{4.58}$$

We now use a Taylor series to expand the square root about $r = 2M - R_0 = f_1$, keeping only the first two non-vanishing terms. This yields

$$u^t \approx \frac{(r + R_0)^2}{r^2 - f_1^2} \left[-\frac{f_1}{r} u + u + \frac{1}{2} \frac{r^2 - f_1^2}{(r + R_0)^2} \frac{1}{u} \right], \tag{4.59}$$

or

$$u^t \approx \frac{(r + R_0)^2}{r (r + f_1)} u + \frac{1}{2u}, \tag{4.60}$$

where all quantities on the right-hand side are evaluated the horizon ($r = 2M - R_0$). We find that, as in maximal trumpet coordinates, u^t is regular at the horizon. For the special case $R_0 = M$, we have $f_1 = M$, so Eqs. (4.56) and (4.60) become

$$u^t = \frac{r + M}{r - M} \left[-\frac{M}{r} u + \left(\frac{r - M}{r + M} + u^2 \right)^{1/2} \right] \tag{4.61}$$

and

$$u^t \approx \frac{r + M}{r} u + \frac{1}{2u}, \tag{4.62}$$

respectively. As before, the normal three-velocity v^r can be computed from Eq. (4.8).

We plot ρ_0, u^t, u^r, and v^r for analytical trumpet coordinates in Fig. 3.1, along with the corresponding solutions for Schwarzschild, isotropic Schwarzschild, and maximal trumpet coordinates. As for maximal trumpets, we find that the solution now extends smoothly inside the black hole horizon, and, as a result, we no longer have to specify artificial initial data in this regime.

Chapter 5

Numerical examples

We have now derived all of the equations necessary to implement the Bondi solution numerically. In this section, we first describe the basics of our numerical code. We then briefly specify the parameters that characterize the particular Bondi solution that we use in our simulations, along with the integration parameters (e.g., grid size and maximum integration time). Finally, we discuss our numerical results using initial data in each of the discussed coordinate systems: isotropic coordinates on slices of constant Schwarzschild time, maximal trumpet coordinates, and analytical trumpet coordinates.

5.1 Numerical code

We use a C++ code that implements the BSSN formulation of Einstein's equations [15–17], together with the equations of relativistic hydrodynamics, in spherical polar coordinates [25, 28, 29]. The code takes as input some type of initial data (which may or may not satisfy the constraint equations; see below) and then solves the evolution equations to evolve that data forward in time. The evolution equations are integrated using a second-order PIRK (partially implicit Runge-Kutta) scheme, without relying on any assumptions of symmetry. One of the ingredients in the BSSN implementation is a so-called reference metric [30, 31]. We distinguish between a "full" approach to solving the equations of relativistic hydrodynamics, in which all fluid equations are expressed in terms of the reference metric, and a "partial" approach, in which the reference metric is

used only for the relativistic Euler equation [Eq. (3.5)]. Both approaches, however, solve all of the equations of relativistic hydrodynamics self-consistently. As discussed below, there are advantages and disadvantages to each approach (see, e.g., [25]); we focus mainly on the partial approach, which, in the case of Bondi accretion, appears to generate smaller errors close to the black hole puncture, where the conformal factor ψ diverges. The code is structured to allow for many different types of initial data, both vacuum and non-vacuum, as well as different slicing and gauge conditions. In our simulations, we use Bondi flow initial data in either isotropic Schwarzschild, maximal trumpet, or analytical trumpet coordinates (Sections 5.2, 5.3, and 5.4, respectively). Our choice for the slicing and gauge conditions depends on the coordinate system.

Each initial data type is described in its own C++ class. My primary contribution to this code consisted of writing the class of initial data used to simulate Bondi accretion. This part of the code is organized as follows. Most of the key equations are implemented in a class called `Bondi_Solution`. In addition, there are three classes that are derived from this class, one for each of the coordinate systems listed above. `Bondi_Solution` contains the equations that are common to all coordinate systems [e.g., Eqs. (4.8) and (4.13) for v^r and u^t, respectively], while the derived classes contain equations that are unique to each coordinate system, such as those for α, β^i, and ψ. Finally, there is a parent class to `Bondi_Solution`, `Bondi`, which in turn is derived from the parent class of all initial data types, `InData`. `Bondi` reads in key parameters (including the coordinate type and values of Γ, $\dot{M}$, and R_s) from an input file, instantiates the appropriate derived class, and facilitates the transfer of information from the ensemble of Bondi classes to the main program.

In all of our simulations we assume a Gamma-law equation of state [Eq. (3.8)] with $\Gamma = 4/3$ and a critical radius of $R_s = 10M$ (see Table 3.1). We choose this value of Γ because it describes a so-called ultra-relativistic gas, in which the internal energy density is large compared to the rest-mass density. We use three different values for the accretion rate, $\dot{M} = 10^{-5}$, $\dot{M} = 10^{-4}$, and $\dot{M} = 10^{-3}$, but focus on the case in which $\dot{M} = 10^{-4}$. All plots included here use $\dot{M} = 10^{-4}$ unless stated otherwise. For simplicity, we take the mass of the black hole to be $M = 1$. We keep the outer boundary

set at $r_{\max} = 64M$, where r is the isotropic radius in our chosen coordinate system, and integrate to a maximum time of $t_{\max} = 64M$. Note that this combination of parameters ensures that the change in mass of the black hole (which, analytically, is equal to the accretion rate multiplied by the integration time) remains small compared to the mass of the black hole. Unless stated otherwise, we use $N_r = 2048$ grid points in the radial direction. Because all solutions are spherically symmetric, we use with the minimum number of angular grid points: $N_\theta = N_\phi = 2$. For plots that show different resolutions at a fixed time, data are taken at $t = 63M$.

5.2 Isotropic Schwarzschild coordinates

We first consider evolutions of Bondi flow in isotropic Schwarzschild coordinates. As discussed in Section 4.3, these coordinates become singular on the black hole horizon at $r = M/2$. As a result, the fluid velocity diverges there when it is expressed in these coordinates (see Fig. 3.1). In order to use initial data expressed in isotropic coordinates, the authors of [10] use artificial initial data inside the horizon ($r \leq M/2$), and modify the initial data in the vicinity of the black hole ($M/2 < r < M$); we will use the same approach here. For the rest-mass density, we fit a quadratic function between $r = M/2$ and $r = M$ such that the radial derivative matches the analytical solution at $r = M$ and goes to zero at $r = M/2$. Inside the horizon, we choose the density to be proportional to $1 - \cos(2\pi r/M)$; at the origin, we set ρ_0 equal to its value at the critical radius, $R = R_s$. For the radial velocity, we let

$$u(r) = u|_{r=M} \times \frac{r}{M} \tag{5.1}$$

for $r < M$. Since the flow is supersonic at $r = M/2$, we expect the initial data inside the horizon to have no affect on the exterior solution. Furthermore, we will see that the solution in this regime quickly settles down to an equilibrium over the course of the evolution.

In order to evolve isotropic Schwarzschild initial data, we employ moving-puncture coordinates, which bring about a coordinate transformation into the maximal trumpet geometry described in Section 4.4. As mentioned in Chapter 4, moving-puncture co-

ordinates are characterized by some variant of the "1 + log" slicing condition for the lapse [18] and a Gamma-driver condition for the shift vector [19]. Here we use a non-advective $1 + \log$ slicing condition,

$$\partial_t \alpha = -2\alpha K, \tag{5.2}$$

where K is the mean curvature, and a non-advective Gamma-driver of the form

$$\begin{aligned} \partial_t \beta^i &= B^i \\ \partial_t B^i &= \frac{3}{4} \partial_t \bar{\Lambda}^i, \end{aligned} \tag{5.3}$$

where $\bar{\Lambda}$ is a so-called connection vector (see, e.g., [28]). Instead of the lapse (4.18) we start with a "pre-collapsed" lapse $\alpha = \psi^{-2}$. (Recall from Section 4.1 that we are free to choose the lapse and shift freely as a result of the coordinate freedom of general relativity; this choice of α proves more useful for numerical simulations that employ moving puncture coordinates.)

In general, the Bondi solution in isotropic Schwarzschild coordinates is time-dependent under the conditions (5.2) and (5.3). In Fig. 5.1 we plot the normal three-velocity $v = -v^r$ [see Eq. (4.8)] as a function of r at different instances of time; as expected, the solution fluctuates over the course of the evolution. Ideally, we would like to be able to compare our numerical solution with an analytical result (e.g., to get a measure of the numerical error). In the case of isotropic initial data evolved with moving puncture coordinates, the only way to do this is by looking at *invariants*, i.e., those quantities that remain time-independent. One such invariant is the rest-mass density ρ_0 plotted as a function of areal radius (Fig. 5.2). We see that the profiles of ρ_0 at each time step fall directly on top of one another, indicating the time-independence of the solution. In addition, the smallest value of the areal radius decreases over the course of the evolution, from $R = 2M$ at $t = 0$ to $R \simeq 1.5M$ at $t = 63M$; this shift is evidence of the transformation from isotropic Schwarzschild coordinates, which terminate on the horizon, to maximal trumpet coordinates, which terminate on a limiting surface of areal radius $R = 1.5M$.

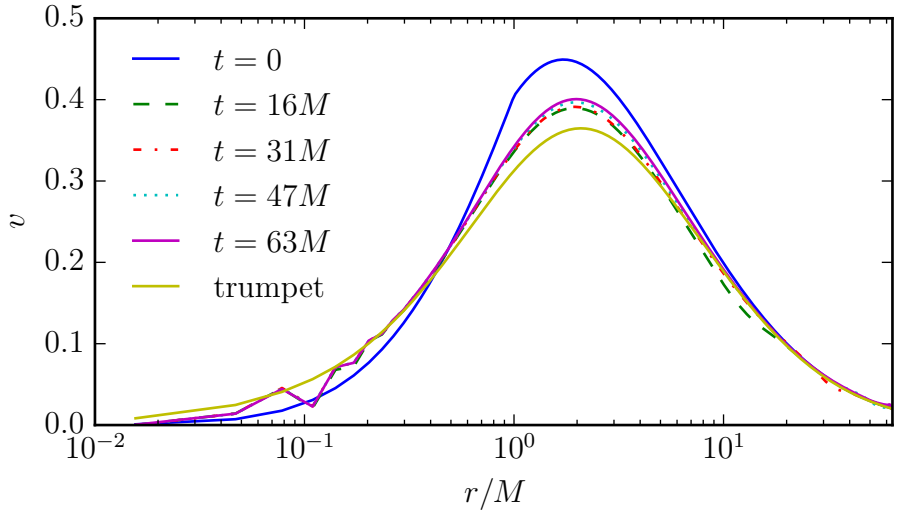

Figure 5.1 Normal three-velocity $v = -v^r$ as a function of isotropic radius r for isotropic Schwarzschild initial data evolved with the 1+log slicing condition (5.2). In contrast to Fig. 5.2, which shows the rest-mass density ρ_0 as a function of R, each of the curves, which represent different time points, are distinct, indicating the time-dependence of the solution. We note some noise in the velocity profile well inside the horizon due to the proximity of the coordinate singularity. Similarly, deviations from the smooth profile at large radii are the result of interactions between the fluid and the outer boundary.

We also plot the lapse α as a function areal radius for isotropic Schwarzschild initial data (Fig. 5.3). Since α describes the geometry of the coordinate system, and the coordinates themselves undergo a transformation during the evolution, we do not expect it to be time-independent. However, we do expect that it converges to the analytical solution for a maximal trumpet; this is what we see in Fig. 5.3. It is important to note that we would not see the same convergent behavior in a plot of α versus the isotropic radius r; this is because r takes on a different meaning as a result of the underlying coordinate transformation.

In general, initial data in isotropic Schwarzschild coordinates are not ideal for simulations that employ moving puncture coordinates. For one, it is necessary to specify artificial initial data in the vicinity of the puncture, and for another, the underlying coordinate transformation makes it difficult to obtain a reliable measure of the numerical error. As we will see in the following two sections, casting the Bondi solution in trumpet coordinates solves both of these issues.

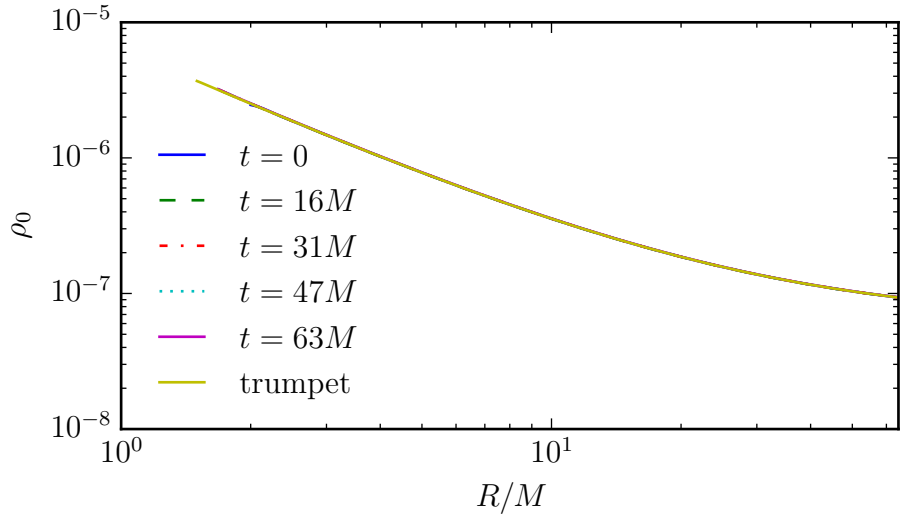

Figure 5.2 Rest-mass density ρ_0 as a function of areal radius R for isotropic Schwarzschild initial data evolved with the $1+\log$ slicing condition (5.2). For the sake of clarity, we eliminate the innermost grid points in this plot, and show only results for the exterior of the black hole throat (see text for details). All of the curves, which correspond to different time points, fall directly on top of one another. However, this does not mean the solution is completely time-independent. Rather, it appears time-independent if we graph gauge-invariant quantities (such as ρ_0) as a function of the areal radius R, which itself has an invariant meaning (see Section 4.2). As expected, the curves also match the analytical solution for a maximal trumpet.

5.3 Maximal trumpets

As discussed in Section 4.4, maximal trumpet coordinates penetrate the black hole horizon smoothly and terminate at a nonzero areal radius $R = 1.5M$. As a result, the fluid variables are all continuous across the horizon and in the vicinity of the puncture (see Fig. 3.1), and it is no longer necessary to specify artificial initial data in that region, as it was in the case of isotropic Schwarzschild coordinates.

We evolve maximal trumpet initial data using the slicing condition (5.2) and gauge condition (5.3), i.e., moving-puncture coordinates. When they act on initial data expressed in maximal trumpet coordinates, these conditions no longer bring about a coordinate transformation, but instead keep the coordinates fixed in a maximal trumpet geometry. We therefore expect that all quantities, not just those that are gauge-invariant, will remain time-independent when expressed in these coordinates.

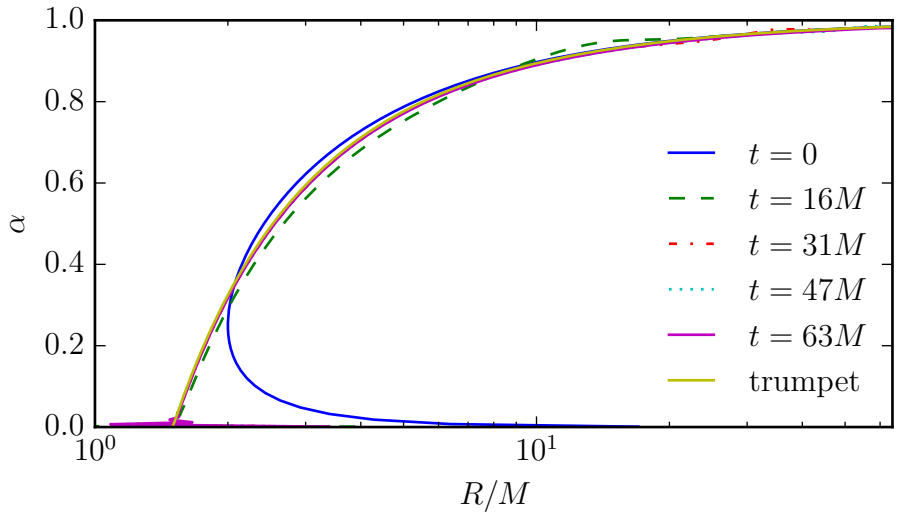

Figure 5.3 Lapse α as a function of areal radius R for isotropic Schwarzschild initial data evolved with the $1 + \log$ slicing condition (5.2). In general, the lapse is time-dependent under this slicing condition. However, it is seen to settle down to the maximal trumpet solution when plotted versus the areal radius. Note that the loop in the $t = 0$ curve back toward larger areal radii is a manifestation of the fact that the isotropic radius is double-valued.

We begin by employing the relativistic Cowling approximation, in which we evolve the fluid but keep the spacetime fixed. In Fig. 5.4 we show the rest-mass density ρ_0 (top panel) and the relative error $\Delta\rho_0/\rho_0$ (bottom panel) for both the partial (left panel) and full (right panel) approaches to solving the equations of relativistic hydrodynamics. To begin with, we find that the relative error obtained using the full approach is less than that obtained using the partial approach at all but the innermost few grid points. In addition, the bottom panels of Fig. 5.4 reveal that, regardless of the approach, the code converges to second order, meaning that the numerical errors decrease with the square of the grid resolution. (In order to demonstrate this behavior, we use grid resolutions $N_r = 256 \times N$ grid points for $N = 1$, 2, 4, and 8, and multiply the errors for each resolution by N^2; the resulting curves converge to one another, demonstrating second order convergence.) With regard to the plots of ρ_0 (top panels), we note that for finer resolutions, the point at which the numerical solution deviates from the analytical solution is closer to the puncture, i.e., we have better agreement over a larger radial range. Note that here and

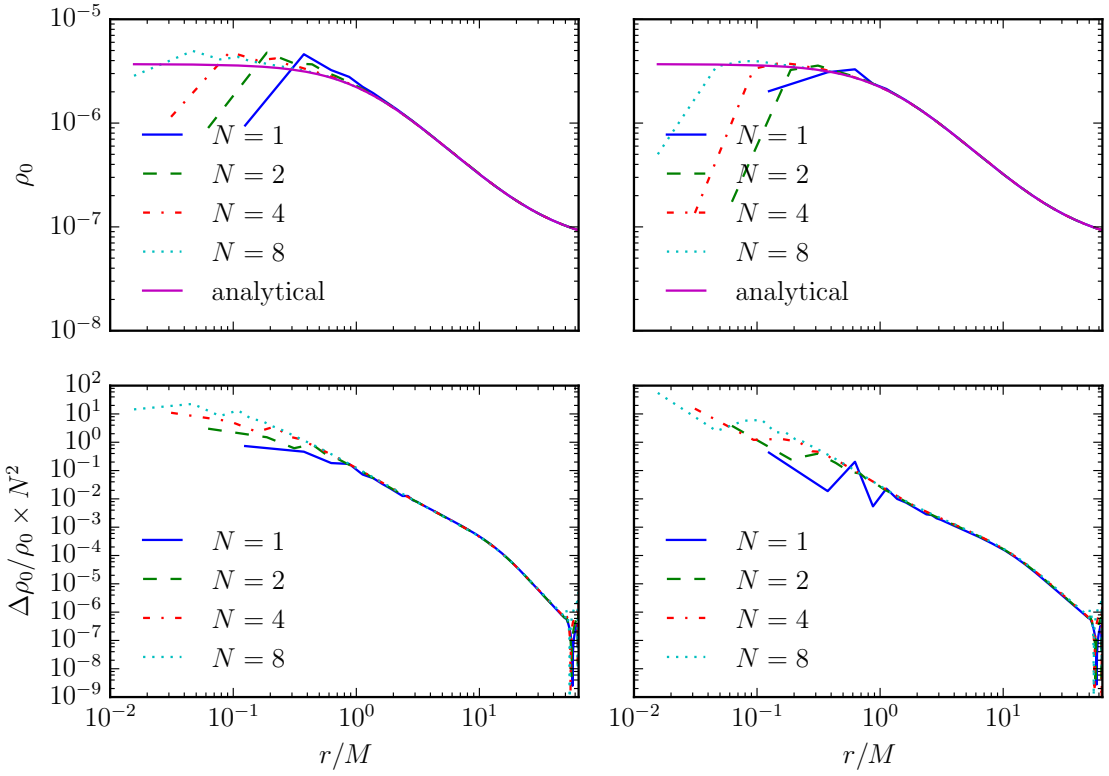

Figure 5.4 Rest-mass density ρ_0 (top panel) and relative error $\Delta\rho_0/\rho_0$ (bottom panel) as a function of isotropic radius r for maximal trumpet initial data evolved in the Cowling approximation. On the left and right we show data obtained using the partial and full approaches, respectively. In each plot the number of radial grid points is given by $N_r = 256 \times N$ for $N = 1$, 2, 4, and 8. We can see in the top panels that for higher resolutions, the point at which our numerical results deviate from the analytical solution is closer to the puncture. (Note that the resolution also affects the placement of the first grid point, i.e., higher resolution curves terminate at smaller minimum radii.) In the bottom panels we have scaled the relative error for each resolution by N^2 to show second-order convergence. We note that the full approach leads to smaller relative errors at all but the innermost few grid points. The dip in the relative error at the right of each of the bottom panels is a numerical artifact caused by interaction of the fluid with the outer boundary.

in all future plots of the rest-mass density ρ_0 (Figs. 5.4 and 5.5), we define the relative error as $\Delta\rho_0/\rho_0 \equiv \left(\rho_0 - \rho_0^{\text{init}}\right)/\rho_0$.

We then switch to evolving the fluid self-consistently with gravitational fields; plots of ρ_0 for these simulations are shown in Fig. 5.5. As before, we plot results for both the partial (left panel) and full (right panel) approaches. For coarse enough resolutions, the code will still converge; however, at finer resolutions, the relative error bottoms out at

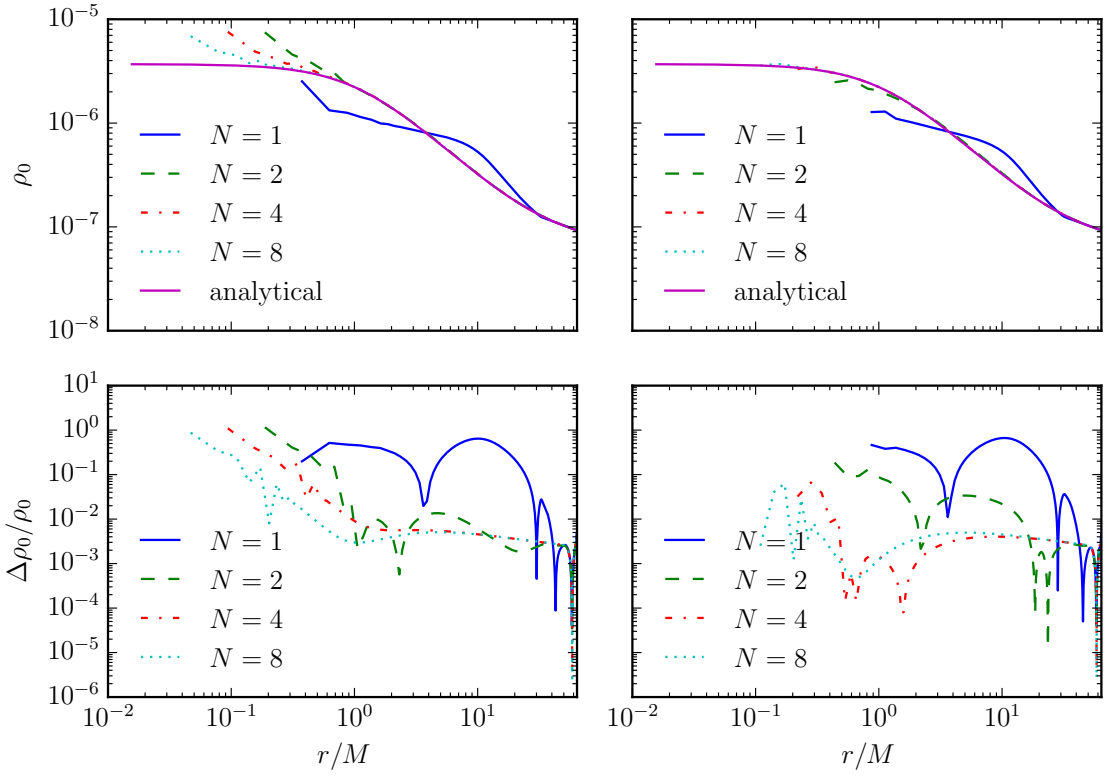

Figure 5.5 Rest-mass density ρ_0 (top panel) and relative error $\Delta\rho_0/\rho_0$ (bottom panel) as a function of isotropic radius r for maximal trumpet initial data evolved self-consistently with the spacetime using the $1 + \log$ slicing condition (5.2). As in Fig. 5.4, we show data obtained using both the partial (left panel) and full (right panel) approaches. The grid resolution is again given by $N_r = 256 \times N$ for $N = 1$, 2, 4, and 8. We note that, in general, the errors in this plot are larger than those obtained using the Cowling approximation. In particular, we find large errors at the first grid point for the partial approach and at the first three grid points for the full approach; for the sake of clarity, we omit those grid points in this plot. We note that, in evolving the spacetime as well as the fluid, we introduce another source of numerical error, namely the fact that our solution is no longer an exact solution to Einstein's equations (i.e., since we neglect the self-gravity of the fluid). We expect this error to be approximately $\dot{M}t/M$, and this is exactly what we see in the bottom panels, in the form of a floor in the relative error at $\Delta\rho_0/\rho_0 \simeq 6 \times 10^{-3}$. We therefore see convergence only as long as the numerical error is dominated by finite-differencing (i.e., for coarser resolutions). Note that, as in Fig. 5.4, finer resolution leads to better agreement closer to the puncture.

$\Delta\rho_0/\rho_0 \simeq 6\times10^{-3}$. This is as expected, since, in turning on the evolution of gravitational fields, we have introduced another source of error due to the fact that the Bondi solution is not an exact solution to Einstein's equations, since it neglects the self-gravity of the fluid. We expect the resultant deviations in the evolved data to scale with the fluid

density, or the accretion rate; specifically, we expect a relative error of approximately $\dot{M}t/M$. As shown in Fig. 5.5, this deviation becomes the dominant source of numerical error for sufficiently fine resolutions (i.e., when the error associated with grid resolution becomes sufficiently small). We note that, in general, the errors obtained using the partial approach are comparable to those obtained using the full approach, except at the innermost few grid points (excluded in the plot), where the errors for the full approach are much larger. For this reason, we choose to employ the partial approach for simulations that evolve both the fluid and spacetime.

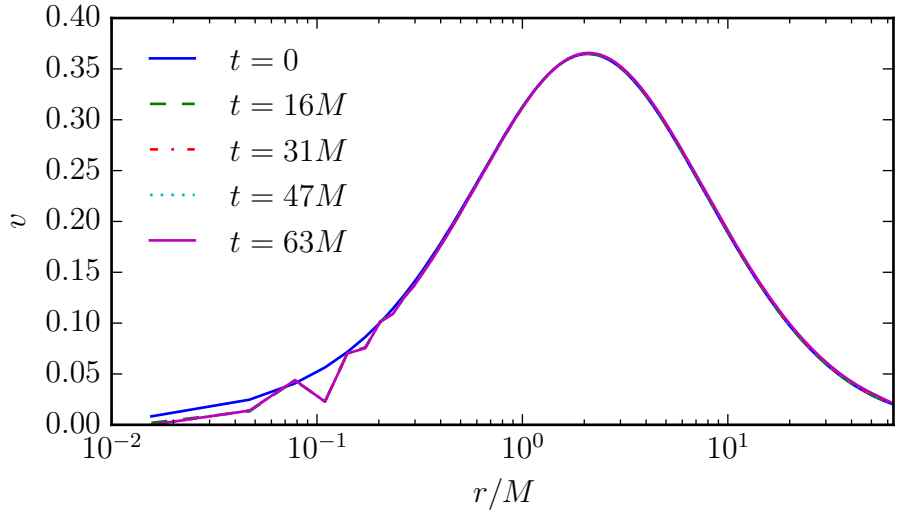

Figure 5.6 Normal three-velocity $v = -v^r$ as a function of isotropic radius r for maximal trumpet initial data evolved with the $1 + \log$ slicing condition. Sufficiently far from the coordinate singularity at the puncture ($r = 0$), profiles of v at different instances of time cannot be distinguished, indicating the time-independence of the solution. (Compare to Fig. 5.1, in which the velocity profile is shown to evolve over the course of the evolution.) We conclude that, by expressing the Bondi solution in maximal trumpet coordinates, it becomes possible to compare all quantities with their analytical counterparts, not only those that are gauge-invariant. As in Fig. 5.1, there is some noise in the profile well inside the horizon; this is due to the proximity of the puncture.

In Fig. 5.6 we plot the normal three-velocity of the fluid as a function of r at different instances of time. As expected, the velocity profile remains approximately constant over the course of the evolution (compare to Fig. 5.1 above), indicating that even gauge-dependent quantities remain time-independent under these coordinate conditions. As a

result, we are able to compare our numerical data directly with the analytical solution, and no longer have to rely solely on invariants as a means of measuring numerical error. We note that the numerical results do diverge slightly from the analytical solution inside the horizon; this is due to the proximity of the coordinate singularity at the puncture.

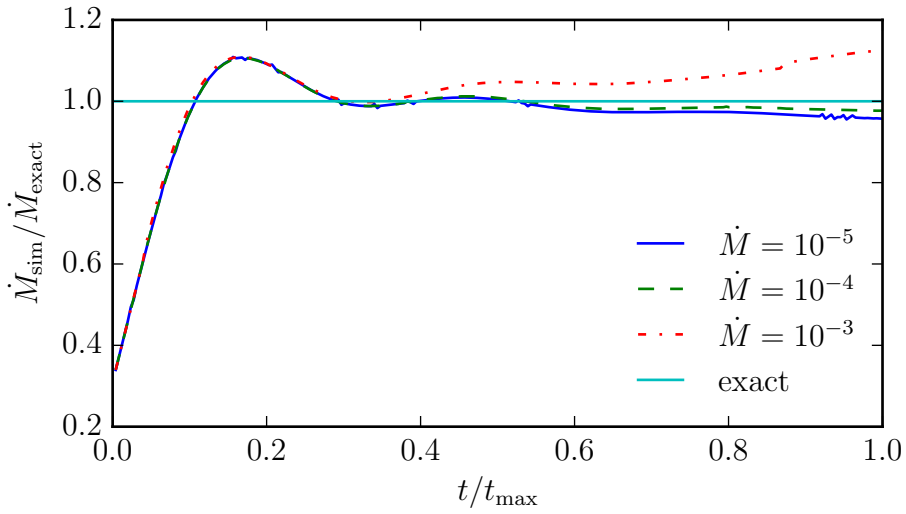

Figure 5.7 Accretion rate $\dot{M}$ as measured by the growth of the event horizon for analytical values $\dot{M} = 10^{-5}$, $\dot{M} = 10^{-4}$, and $\dot{M} = 10^{-3}$, plotted as a function of time. Initial data are given in maximal trumpet coordinates and evolved using the moving-puncture method. In order to directly compare our results for different accretion rates, we normalize the computed value of $\dot{M}$ ($\dot{M}_{\rm sim}$) by the corresponding analytical value ($\dot{M}_{\rm exact}$). For all values of $\dot{M}$, there is an initial period of adjustment ($0 < t < 0.4t_{\rm max}$) before the solution settles down into an approximately steady state. We might expect smaller values of $\dot{M}$ (i.e., lower densities) to result in better agreement with the exact solution; the fact that this does not occur may be the result of numerical uncertainty in horizon-finding process. To obtain these data we used a resolution of $N_r = 256$ on a logarithmic grid.

Finally, in Fig. 5.7, we show the accretion rate, which is computed in our numerical code from the growth of the event horizon, as a function of time for several different values of $\dot{M}$. In each case, we normalize the numerical value ($\dot{M}_{\rm sim}$) by the corresponding analytical value ($\dot{M}_{\rm exact}$) in order to directly compare our results. (Note that $\dot{M}$ is an input parameter and, as such, does not change over the course of the evolution. However, due to numerical effects, there is a discrepancy between the measured value of

the accretion rate and the value of $\dot{M}$.) While we do not necessarily see convergence for decreasing $\dot{M}$, all curves do approach the analytical value after an initial period of flux.

5.4 Analytical trumpets

As for maximal trumpet coordinates, spatial slices in an analytical trumpet geometry penetrate the black hole horizon smoothly and terminate on a limiting surface at a nonzero distance (as measured in areal radius) from the spacetime singularity. Recall that analytical trumpet coordinates encompass a family of coordinate systems that are parameterized by the value R_0, where $0 \leq R_0 \leq M$. In our numerical simulations, we consider the member of this family corresponding to $R_0 = M$, for which the limiting surface occurs at an areal radius $R = M$. In these coordinates, the fluid variables are all well-behaved at the horizon (see Fig. 3.1), and it is not necessary to specify artificial initial data close to the puncture.

In order to evolve initial data in analytical trumpet coordinates, we use a variation of the $1 + \log$ slicing condition given by

$$\partial_t \alpha = -\alpha \left(1 - \alpha\right) K, \tag{5.4}$$

and a non-advective Gamma-driver condition for the shift (5.3). As mentioned in [23], the slicing condition (5.4) can lead to coordinate pathologies. However, as shown below, we are nonetheless able to carry out simulations of Bondi accretion using initial data expressed in these coordinates. We expect data given in analytical trumpet coordinates to remain time-independent under the above coordinate conditions.

All of the key results discussed above in the context of maximal trumpet coordinates (notably the time-independence of both gauge-independent and gauge-dependent quantities) also apply, in general, to simulations in analytical trumpet coordinates. In Fig. 5.8 we show snapshots of the normal three-velocity of the fluid as a function of r at different instances of time. As in the analogous plot for maximal trumpet initial data (Fig. 5.6), and in contrast to that for isotropic Schwarzschild initial data (Fig. 5.1), all of

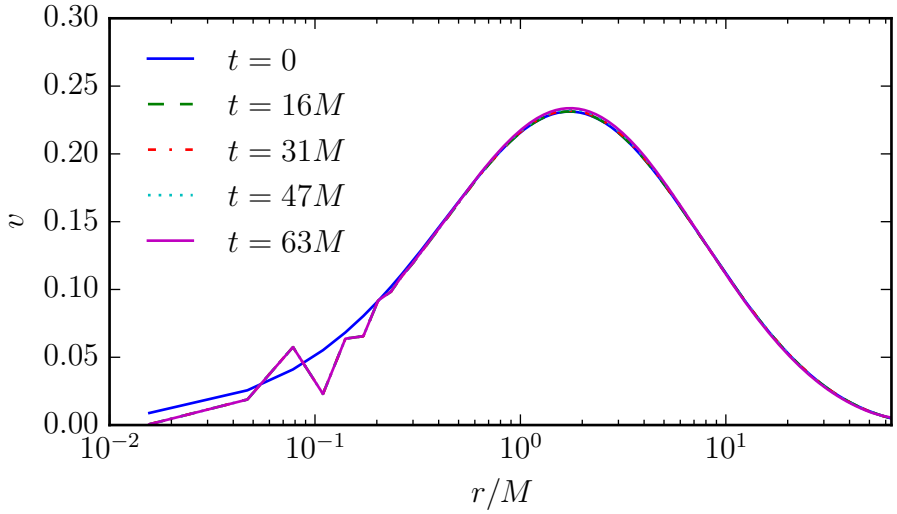

Figure 5.8 Normal three-velocity $v = -v^r$ as a function of isotropic radius r for analytical trumpet initial data evolved with the $1 + \log$ slicing condition (5.4). Once again, profiles at different instances of time overlap very closely, demonstrating the time-independence of the solution. We observe slightly larger errors than we did for maximal trumpets (Fig. 5.6); this discrepancy is most clearly visible at the peak of the velocity profile. However, we still find that the numerical results converge to the analytical solution with increasing resolution. Once again, the noise at small radii inside the horizon is a numerical artifact caused by interaction with the puncture.

the curves fall on top of one another, indicating the time-independence of the solution. As in Fig. 5.6, we observe small discrepancies between the numerical and analytical solutions at small radii; this is again due to the proximity of the coordinate singularity at $r = 0$. Finally, we note that, in general, analytical trumpet coordinates lead to slightly larger errors than maximal trumpets. (In Figs. 5.6 and 5.8, this discrepancy is most visible at the peak of the profile.) However, in both cases we find that the numerical data converge to the analytical solution with increasing resolution.

Chapter 6

Summary

The Bondi solution, which was originally derived by Hermann Bondi in 1952, describes spherically symmetric, radial accretion onto a non-rotating black hole in the fluid limit. Because it can be understood analytically, this solution serves as a powerful test for relativistic hydrodynamics and magnetohydrodynamics codes. The original Bondi solution is formulated in Schwarzschild coordinates (Chapter 3), which, while convenient from an analytical point of view, cannot be implemented numerically. As a result, numerical simulations of Bondi accretion (or at least those that evolve the fluid and spacetime self-consistently) typically cast the solution in isotropic Schwarzschild coordinates (Section 4.3) and then evolve it using so-called moving-puncture coordinates (Section 4.4), which induce a transition into a trumpet geometry. Trumpet coordinates have proven to be very useful in numerical simulations of black hole spacetimes. For one, they penetrate the black hole horizon smoothly, thereby avoiding issues that arise there in other coordinate systems. In addition, they terminate on a limiting surface of nonzero areal radius, thus avoiding problems associated with the spacetime singularity.

Here we transform the Bondi solution into two different trumpet coordinate systems. In the new coordinates, the Bondi solution is no longer singular at the horizon, and remains time-independent when evolved with moving-puncture coordinates. We demonstrate the usefulness of this solution in several numerical examples. In particular, we show that all quantities, not just those that are gauge-invariant, remain time-independent over

the course of the evolution. As a result, we can more easily determine and characterize the numerical error associated with our simulations.

Appendices

Appendix A

Notes on Newtonian Bondi accretion

In this appendix, we continue the discussion of non-relativistic Bondi accretion presented in Chapter 2. First, in Section A.1, we derive an equation for the accretion rate $\dot{M}$ in terms of the boundary values at infinity. Then, in Section A.2, we consider the behavior of the fluid in the limits $r \gg r_s$ and $r \ll r_s$.

A.1 Computing $\dot{M}$ in terms of boundary values

We start by using the Bernoulli equation (2.24) to express the sonic radius r_s in terms of the sound speed at infinity. Recall that at the sonic radius

$$u_s^2 = a_s^2 = \frac{1}{2}\frac{GM}{r_s} \tag{A.1}$$

[cf. Eq. (2.18)]. Inserting this equation into (2.24) gives

$$\frac{1}{4}\frac{GM}{r_s} + \frac{1}{2\,(\Gamma-1)}\frac{GM}{r_s} - \frac{GM}{r_s} = \frac{1}{\Gamma-1}a_\infty^2, \tag{A.2}$$

which can be rearranged to obtain

$$a_\infty^2 = \left(\frac{5-3\Gamma}{4}\right)\frac{GM}{r_s}, \tag{A.3}$$

or

$$r_s = \left(\frac{5-3\Gamma}{4}\right)\frac{GM}{a_\infty^2} \tag{A.4}$$

[cf. Eq. (ST.14.3.14)]. Substituting (A.4) into (A.1) yields

$$u_s^2 = a_s^2 = \left(\frac{2}{5-3\Gamma}\right)a_\infty^2. \tag{A.5}$$

We now want to express the density ρ in terms of a and the boundary values ρ_∞ and a_∞. From our equation for the sound speed (2.2) we have

$$a^2 = \frac{\Gamma P}{\rho} = \Gamma\kappa\rho^{\Gamma-1}, \tag{A.6}$$

or

$$\rho = \left(\frac{a^2}{\Gamma\kappa}\right)^{1/(\Gamma-1)}. \tag{A.7}$$

This implies $\rho \propto a^{2/(\Gamma-1)}$, so

$$\frac{\rho}{\rho_\infty} = \left(\frac{a}{a_\infty}\right)^{2/(\Gamma-1)} \tag{A.8}$$

[cf. Eq. (ST.14.3.15)]. Inserting (A.8) into our equation for the accretion rate (2.19) and evaluating at the sonic radius yields

$$\dot{M} = 4\pi\rho_\infty a_s r_s^2\left(\frac{a_s}{a_\infty}\right)^{2/(\Gamma-1)}, \tag{A.9}$$

where we have also substituted $u_s = a_s$. We can now insert Eqs. (A.4) and (A.5) for r_s and a_s, respectively, to obtain

$$\dot{M} = 4\pi\lambda_s\left(\frac{GM}{a_\infty}\right)^2\rho_\infty a_\infty \tag{A.10}$$

[cf. Eq. (ST.14.3.16)], where $\lambda_s = \lambda_s(\Gamma)$ is the so-called accretion eigenvalue for the transonic solution,

$$\lambda_s = \left(\frac{1}{2}\right)^{(\Gamma+1)/2(\Gamma-1)}\left(\frac{5-3\Gamma}{4}\right)^{-(5-3\Gamma)/2(\Gamma-1)} \tag{A.11}$$

[cf. Eq. (ST.14.3.17)]. Values of λ_s for several different Γ, $1 \geq \Gamma \geq 5/3$, are given in Table 14.1 of [4]. In our numerical simulations we use $\Gamma = 4/3$, which corresponds to $\lambda_s \simeq 0.707$.

A.2 Fluid profiles in the limits $r \gg r_s$ and $r \ll r_s$

We will now calculate the flow profiles for the transonic solution in the limits $r \gg r_s$ and $r \ll r_s$. In order to calculate the temperature profile, we specialize to the case of a Maxwell-Boltzmann gas of mean molecular weight μ. In this case the pressure is given by

$$P = \frac{\rho \kappa T}{\mu m_u}, \tag{A.12}$$

where T is the temperature and m_u is the atomic mass. Inserting (A.12) into our equation for the sound speed (2.2) gives

$$a^2 = \frac{\Gamma P}{\rho} = \frac{\Gamma \kappa T}{\mu m_u}. \tag{A.13}$$

The temperature is therefore proportional to the sound speed squared, so

$$\frac{T}{T_\infty} = \left(\frac{a}{a_\infty}\right)^2 = \left(\frac{\rho}{\rho_\infty}\right)^{\Gamma - 1} \tag{A.14}$$

[cf. Eq. (ST.14.3.19)], where we have used Eq. (A.8) in the final equality. For $r \gg r_s$, the gravitational potential of the black hole is negligible, and the density, temperature, and sound speed remain close to their asymptotic values:

$$\rho \approx \rho_\infty, \qquad T \approx T_\infty, \qquad a \approx a_\infty, \qquad \frac{r}{r_s} \gg 1 \tag{A.15}$$

[cf. Eq. (ST.14.3.21)]. We can calculate the velocity profile in this limit by combining Eqs. (2.19) and (A.10) to obtain

$$\dot{M} = 4\pi r^2 \rho u = 4\pi \lambda_s \left(\frac{GM}{a_\infty^2}\right)^2 \rho_\infty a_\infty. \tag{A.16}$$

Since $\rho \approx \rho_\infty$ for $r \gg r_s$ [Eq. (A.15)], this yields

$$\frac{u}{a_\infty} \approx \lambda_s \left(\frac{GM}{a_\infty^2}\right) r^{-2}, \qquad \frac{r}{r_s} \gg 1 \tag{A.17}$$

[cf. Eq. (ST.14.3.22)].

In the limit $r \ll r_s$, the fluid is significantly influenced by the gravitational field of the black hole; the deceleration of the fluid due to gas pressure becomes negligible and u approaches the free-fall velocity. In Eq. (2.24), the term GM/r dominates over the term $a^2/(\Gamma - 1)$, giving

$$u \approx \left(\frac{2GM}{r}\right)^{1/2}, \qquad \frac{r}{r_s} \ll 1 \qquad \left(1 \le \Gamma < \frac{5}{3}\right) \tag{A.18}$$

[cf. Eq. (ST.14.3.23)]. The density profile can be calculated from Eqs. (A.16) and (A.18). From (A.16) we have

$$\frac{\rho}{\rho_\infty} = \lambda_s \left(\frac{GM}{a_\infty^2}\right) a_\infty r^{-2} u^{-1}. \tag{A.19}$$

which, when combined with Eq. (A.18) for the fluid velocity, yields

$$\frac{\rho}{\rho_\infty} = \frac{\lambda_s}{2^{1/2}} \left(\frac{GM}{a_\infty^2}\right)^{3/2} r^{-3/2}, \qquad \frac{r}{r_s} \ll 1 \qquad \left(1 \le \Gamma < \frac{5}{3}\right) \tag{A.20}$$

[cf. Eq. (ST.14.3.24)]. The temperature profile in the limit $r \ll r_s$ can be found by inserting our expression for the ρ/ρ_∞ (A.20) into Eq. (A.14). This yields

$$\frac{T}{T_\infty} \approx \left[\frac{\lambda_s}{2^{1/2}} \left(\frac{GM}{a_\infty^2}\right)^{3/2}\right]^{\Gamma-1} r^{-3(\Gamma-1)/2}, \qquad \frac{r}{r_s} \ll 1 \qquad \left(1 \le \Gamma < \frac{5}{3}\right) \tag{A.21}$$

[cf. Eq. (ST.14.3.25)]. Note that Eqs. (A.18), (A.20), and (A.21) are also true in the relativistic case if we identify r with the Schwarzschild radius, u with the radial component of the four-velocity, and ρ with the proper rest-mass density [cf. Eqs. (B.19), (B.21), and (B.24)].

These same three equations are altered slightly in the case $\Gamma = 5/3$. In the Newtonian approximation, $\Gamma = 5/3$ corresponds to a transonic radius of $r_s = 0$ [see Eq. (A.4)], which

means that we can use Eq. (2.18), which describes the flow at the transonic radius, to approximate the flow at small radii $r/\left(GM/a_\infty^2\right) \ll 1$. We therefore have

$$a \approx u \approx \left(\frac{GM}{2r}\right)^{1/2}, \qquad \frac{r}{GM/a_\infty^2} \ll 1 \qquad \left(\Gamma = \frac{5}{3}\right) \tag{A.22}$$

[cf. Eq. (ST.14.3.26)]. In analogy to the more general case described above, we can calculate the density profile from Eqs. (A.19) and (A.22). Inserting Eq. (A.22) for the fluid velocity into Eq. (A.19) yields

$$\frac{\rho}{\rho_\infty} \approx \frac{1}{2^{3/2}} \left(\frac{GM}{a_\infty^2}\right)^{3/2} r^{-3/2}, \qquad \frac{r}{GM/a_\infty^2} \ll 1 \qquad \left(\Gamma = \frac{5}{3}\right), \tag{A.23}$$

where we have substituted $\lambda_s = 1/4$ for $\Gamma = 5/3$. Inserting (A.23) into (A.14) gives the temperature profile,

$$\frac{T}{T_\infty} \approx \frac{1}{2} \left(\frac{GM}{a_\infty^2}\right) r^{-1}, \qquad \frac{r}{GM/a_\infty^2} \ll 1 \qquad \left(\Gamma = \frac{5}{3}\right) \tag{A.24}$$

[cf. Eq. (ST.14.3.27)]. In the relativistic case, Eqs. (A.22), (A.23), and (A.24) are multiplied by numerical factors of order unity [cf. Eqs. (B.36), (B.37), and (B.38)].

Appendix B

Notes on relativistic Bondi accretion

In this appendix, we continue where we left off in our discussion of relativistic Bondi accretion in Chapter 3. We first show how to calculate the accretion rate $\dot{M}$ in terms of the boundary values ρ_∞ and a_∞ (Section B.1), and then derive expressions for the fluid variables in the limit $R \ll R_s$ and at the horizon (Section B.2).

B.1 Computing $\dot{M}$ in terms of boundary values

We begin by using the relativistic Bernoulli equation (3.53) to relate a_s, the sound speed at the critical radius, and a_∞, the sound speed at infinity. Evaluating the left side of Eq. (3.53) at $R = R_s$, and using Eqs. (3.33) and (3.34) to express u_s and R_s in terms of a_s, we obtain

$$\left(\frac{\Gamma-1}{\Gamma-1-a_s^2}\right)^2\left(\frac{1}{1+3a_s^2}\right) = \left(\frac{\Gamma-1}{\Gamma-1-a_\infty^2}\right)^2, \tag{B.1}$$

or, taking the inverse of both sides,

$$\left(1-\frac{a_s^2}{\Gamma-1}\right)^2\left(1+3a_s^2\right) = \left(1-\frac{a_\infty^2}{\Gamma-1}\right)^2 \tag{B.2}$$

[cf. Eq. (ST.G.30)]. At large radii $R \geq R_s$, we expect the fluid particles to be non-relativistic ($a \leq a_s \ll 1$), provided they were non-relativistic at infinity ($a_\infty \ll 1$). In order to solve for a_s in terms of a_∞, we expand (B.2) to lowest non-vanishing order in a_s^2 and a_∞^2. Here and in the calculations that follow, we must be careful to distinguish

the cases $\Gamma \neq 5/3$ and $\Gamma = 5/3$. For the more general case $\Gamma \neq 5/3$, we can expand the left-hand side of (B.2) as

$$\left(1 - \frac{a_s^2}{\Gamma - 1}\right)^2 \left(1 + 3a_s^2\right) \approx \left(1 - \frac{2a_s^2}{\Gamma - 1}\right) \left(1 + 3a_s^2\right) \approx 1 + \frac{3\Gamma - 5}{\Gamma - 1} a_s^2. \tag{B.3}$$

Notice that for $\Gamma = 5/3$ the term $(3\Gamma - 5) / (\Gamma - 1)$ vanishes, and we must expand to higher order [see Eq. (B.7) below]. Expanding the right side of Eq. (B.2) gives, for $\Gamma \neq 5/3$,

$$\left(1 - \frac{a_\infty^2}{\Gamma - 1}\right)^2 \approx 1 - \frac{2}{\Gamma - 1} a_\infty^2. \tag{B.4}$$

Thus, we have

$$1 + \frac{3\Gamma - 5}{\Gamma - 1} a_s^2 \approx 1 - \frac{2}{\Gamma - 1} a_\infty^2, \tag{B.5}$$

or

$$a_s^2 \approx \frac{2}{5 - 3\Gamma} a_\infty^2 \qquad \left(\Gamma \neq \frac{5}{3}\right) \tag{B.6}$$

[cf. Eq. (ST.G.31)]. We now consider the special case $\Gamma = 5/3$. Expanding the left side of Eq. (B.2), this time to order a_s^4, gives

$$\left(1 - \frac{3}{2} a_s^2\right)^2 \left(1 + 3a_s^2\right) = \left(1 - 3a_s^2 + \frac{9}{4} a_s^4\right) \left(1 + 3a_s^2\right) \approx 1 - \frac{27}{4} a_s^4, \tag{B.7}$$

while on the right side we have

$$\left(1 - \frac{3}{2} a_\infty^2\right)^2 \approx 1 - 3a_\infty^2. \tag{B.8}$$

Thus, for $\Gamma = 5/3$, we have

$$1 - \frac{27}{4} a_s^4 \approx 1 - 3a_\infty^2, \tag{B.9}$$

or

$$a_s^2 \approx \frac{2}{3} a_\infty \qquad \left(\Gamma = \frac{5}{3}\right) \tag{B.10}$$

[cf. Eq. (ST.G.31)]. We can now use Eqs. (B.6) and (B.10) in combination with (3.33) to solve for R_s in terms of a_∞. Rearranging (3.33) to solve for R_s gives

$$R_s = M\left(\frac{1+3a_s^2}{2a_s^2}\right). \tag{B.11}$$

Then, for $\Gamma \neq 5/3$, we have

$$R_s \approx \frac{5-3\Gamma}{4}\frac{M}{a_\infty^2}\left(1+\frac{6}{5-3\Gamma}a_\infty^2\right) \approx \frac{5-3\Gamma}{4}\frac{M}{a_\infty^2} \qquad \left(\Gamma \neq \frac{5}{3}\right), \tag{B.12}$$

where to obtain the final expression we have taken the term in parentheses to be ≈ 1, since we are assuming $a_\infty^2 \ll 1$. For $\Gamma = 5/3$, we have

$$R_s \approx \frac{3}{4}\frac{M}{a_\infty}\left(1+2a_\infty\right) \approx \frac{3}{4}\frac{M}{a_\infty} \qquad \left(\Gamma = \frac{5}{3}\right), \tag{B.13}$$

where we have again used the fact that $a_\infty \ll 1$ to simplify our result. We now use Eq. (3.51) to relate the rest-mass density at the critical radius, $\rho_{0,s}$, to the rest-mass density at infinity, $\rho_{0,\infty}$. For large radii $R \geq R_s$ ($a \ll 1$), Eq. (3.51) simplifies to

$$\Gamma\kappa\rho_0^{\Gamma-1} \approx a^2, \tag{B.14}$$

which implies $\rho_0 \propto a^{2/(\Gamma-1)}$. Thus,

$$\frac{\rho_{0,s}}{\rho_{0,\infty}} \approx \left(\frac{a_s}{a_\infty}\right)^{2/(\Gamma-1)} \tag{B.15}$$

[cf. Eq. (ST.G.32)].

We can now use Eqs. (3.34), (3.36), (B.6), (B.12), and (B.15) to express the accretion rate $\dot{M}$ in terms of the boundary values at infinity, a_∞ and $\rho_{0,\infty}$. Evaluating (3.36) at $R = R_s$ gives

$$\dot{M} = 4\pi\rho_{0,s}u_s R_s^2. \tag{B.16}$$

Rewriting $\rho_{0,s}$, u_s, and R_s in terms of a_∞ and $\rho_{0,\infty}$ according to above equations, we obtain

$$\dot{M} = 4\pi\lambda_s M^2 \rho_{0,\infty} a_\infty^{-3} \tag{B.17}$$

[cf. Eq. (ST.G.33)], where $\lambda_s = \lambda_s(\Gamma)$ is given by

$$\lambda_s = \left(\frac{1}{2}\right)^{(\Gamma+1)/2(\Gamma-1)} \left(\frac{5-3\Gamma}{4}\right)^{-(5-3\Gamma)/2(\Gamma-1)} \tag{B.18}$$

[cf. Eq. (ST.14.3.7)]. Note that to lowest order, the relativistic accretion rate (B.17) is equal to the accretion rate for Newtonian (i.e., non-relativistic) Bondi flow [cf. Eq. (A.10)]. The equivalence of these two results is physically reasonable, since the critical accretion rate is determined by the fluid parameters at $R = R_s$, which is far from the event horizon of the black hole ($R_s \gg 2M$) and thus, to reasonable approximation, uninfluenced by non-linear gravity.

B.2 Fluid profiles in the limit $R \ll R_s$

We now investigate the behavior of the gas in the limit $R \ll R_s$. We can estimate the fluid velocity in this limit using Eq. (3.53). The first term on the left-hand side and the sole term on the right-hand side both remain finite in the limit $R \ll R_s$. Therefore, the middle term must also remain finite. Since $2M/R$ diverges to infinity as $R \to 0$, we conclude that u^2 must diverge in the same way. That is,

$$u^2 \approx \frac{2M}{R}, \qquad R \ll R_s \qquad \left(\Gamma \neq \frac{5}{3}\right) \tag{B.19}$$

[cf. Eq. (ST.G.34)]. The u^2 and $2M/R$ terms will now cancel, and both sides of the equation will remain finite in the limit $R \ll R_s$. We now want to obtain an expression for the compression of the gas at small radii. Combining Eqs. (B.16) and (B.17) yields

$$\frac{\rho_0}{\rho_{0,\infty}} \approx \lambda_s M^2 a_\infty^{-3} u^{-1} R^{-2}, \tag{B.20}$$

or, inserting Eq. (B.19) for the fluid velocity,

$$\frac{\rho_0}{\rho_{0,\infty}} \approx \frac{\lambda_s}{2^{1/2}} \left(\frac{M}{a_\infty^2 R}\right)^{3/2}, \qquad R \ll R_s \qquad \left(\Gamma \neq \frac{5}{3}\right) \tag{B.21}$$

[cf. Eq. (ST.G.35)]. If we assume the fluid to be a Maxwell-Boltzmann gas with pressure $P = \rho_0 kT$, then we can calculate the temperature profile from the equation of state (3.14). Combining these two relations yields

$$P = \rho_0 kT = \kappa \rho_0^\Gamma, \tag{B.22}$$

from which we can discern that $T \propto \rho_0^{\Gamma-1}$. Thus,

$$\frac{T}{T_\infty} = \left(\frac{\rho_0}{\rho_{0,\infty}}\right)^{\Gamma-1}, \tag{B.23}$$

or, substituting Eq. (B.21) for the rest-mass density,

$$\frac{T}{T_\infty} \approx \left(\frac{\lambda_s}{2^{1/2}}\right)^{\Gamma-1} \left(\frac{M}{a_\infty^2 R}\right)^{3/2(\Gamma-1)}, \qquad R \ll R_s \qquad \left(\Gamma \neq \frac{5}{3}\right) \tag{B.24}$$

[cf. Eq. (ST.G.36)].

We can also calculate the fluid velocity, compression, and temperature at the horizon by evaluating the above equations at $R = 2M$. From Eqs. (B.19), (B.21), and (B.24), respectively, we obtain

$$u_h \approx 1 \qquad \left(\Gamma \neq \frac{5}{3}\right), \tag{B.25}$$

$$\frac{\rho_{0,h}}{\rho_{0,\infty}} \approx \frac{\lambda_s}{4} \left(\frac{c}{a_\infty}\right)^3 \qquad \left(\Gamma \neq \frac{5}{3}\right), \tag{B.26}$$

and

$$\frac{T_h}{T_\infty} \approx \left[\frac{\lambda_s}{4} \left(\frac{c}{a_\infty}\right)^3\right]^{\Gamma-1} \qquad \left(\Gamma \neq \frac{5}{3}\right) \tag{B.27}$$

[cf. Eq. (ST.G.37)], where in the last two equations we have reinserted c, the speed of light. Note that all three of these equations are independent of the black hole mass M.

Eqs. (B.25), (B.26), and (B.27) are slightly modified in the special case $\Gamma = 5/3$. In this case, a remains comparable to u inside the transonic radius ($R < R_s$). From Eq. (B.10), we know that $a^2 \sim a_\infty$. As a result, we can neglect all terms in Eq. (3.53) that are of order a_∞^2, in which case the right-hand side reduces to unity. Inserting $R = 2M$ and $\Gamma = 5/3$ and evaluating at the horizon then yields

$$u_h \left(1 + \frac{a_h^2}{\frac{2}{3} - a_h^2} \right) \approx 1 \tag{B.28}$$

[cf. Eqs. (ST.G.38)]. We now want to express a_h in terms of the rest-mass density at the horizon, $\rho_{0,h}$. Evaluating Eq. (3.50) at the horizon gives

$$a_h^2 = \frac{\frac{5}{3}\kappa\rho_{0,h}^{2/3}}{1 + \frac{5}{2}\kappa\rho_{0,h}^{2/3}} \tag{B.29}$$

for $\Gamma = 5/3$. Inserting this expression into (B.28) then yields

$$u_h \left(1 + \frac{5}{2}\kappa\rho_{0,h}^{2/3} \right) \approx 1 \tag{B.30}$$

[cf. Eqs. (ST.G.39)]. We can use Eqs. (3.36) and (B.17) to solve for $\rho_{0,h}$ in terms of the boundary values at infinity. Combining these two equations and evaluating at the horizon yields

$$\rho_{0,h} = \frac{\lambda_s}{4} \frac{\rho_{0,\infty}}{a_\infty^3 u_h} = \frac{\rho_{0,\infty}}{16 a_\infty^3 u_h} \tag{B.31}$$

[cf. Eqs. (ST.G.40)], where in the last equality we have inserted $\lambda_s = 1/4$ for $\Gamma = 5/3$. We use Eq. (3.50) to express a_∞ in terms of ρ_∞. For $\Gamma = 5/3$, this gives

$$a_\infty^2 = \frac{\frac{5}{3}\kappa\rho_{0,\infty}^{2/3}}{1 + \frac{5}{2}\kappa\rho_{0,\infty}^{2/3}} \approx \frac{5}{3}\kappa\rho_{0,\infty}^{2/3} \tag{B.32}$$

[cf. Eqs. (ST.G.41)]. Note that the final approximation is justified because we are assuming $\rho_{0,\infty} \ll 1$. We can now use Eqs. (B.31) and (B.32) to rewrite the density term in (B.30) as

$$\frac{5}{2}\kappa\rho_{0,h}^{2/3} = \frac{5}{2} \frac{\kappa\rho_{0,\infty}^{2/3}}{16^{2/3} a_\infty^2 u_h} = \frac{3}{2^{11/3}} u_h^{-2/3}. \tag{B.33}$$

Making this substitution in Eq. (B.30) yields

$$u_h \left(1 + \frac{3}{2^{11/3}} u_h^{-2/3}\right) \approx 1, \tag{B.34}$$

or

$$u_h + \frac{3}{2^{11/3}} u_h^{1/3} \approx 1 \tag{B.35}$$

[cf. Eq. (ST.G.42)], which can be solved numerically to find

$$u_h \approx 0.782 \qquad \left(\Gamma = \frac{5}{3}\right). \tag{B.36}$$

[cf. Eq. (ST.G.43)]. Using Eq. (B.31), we can write the gas compression at the horizon as

$$\frac{\rho_{0,h}}{\rho_{0,\infty}} \approx \frac{1}{16 u_h} \left(\frac{c}{a_\infty}\right)^3 \qquad \left(\Gamma = \frac{5}{3}\right). \tag{B.37}$$

The temperature is then given by

$$\frac{T_h}{T_\infty} = \left(\frac{\rho_{0,h}}{\rho_{0,\infty}}\right)^{2/3} \approx \left(\frac{1}{16 u_h}\right)^{2/3} \left(\frac{c}{a_\infty}\right)^2 \qquad \left(\Gamma = \frac{5}{3}\right) \tag{B.38}$$

[cf. Eq. (ST.G.44)].

Appendix C

Derivation of the relativistic Euler equation

In this appendix we derive the relativistic Euler equation,

$$(\rho + P)\, u^b \nabla_b u^a = -\partial^a P - u^a u^b \partial_b P \tag{C.1}$$

[cf. Eq. (3.5)], from the conservation of energy-momentum,

$$\nabla_a T^{ab} = 0 \tag{C.2}$$

[cf. Eq. (3.3)]. We take T^{ab} to be the stress-energy tensor for a perfect fluid,

$$T^{ab} = (\rho + P)\, u^a u^b + P g^{ab}. \tag{C.3}$$

We begin by evaluating the divergence of T^{ab}. Inserting (C.3) into (C.2) gives

$$\begin{aligned} \nabla_b T^{ab} &= \nabla_b \left[(\rho + P)\, u^a u^b + P g^{ab} \right] \\ &= u^a u^b \nabla_b (\rho + P) + (\rho + P)\, u^b \nabla_b u^a + (\rho + P)\, u^a \nabla_b u^b + g^{ab} \nabla_b P, \end{aligned} \tag{C.4}$$

or, contracting with u_a,

$$u_a \nabla_b T^{ab} = u_a u^a u^b \nabla_b (\rho + P) + (\rho + P) u_a u^b \nabla_b u^a + (\rho + P) u_a u^a \nabla_b u^b + u^b \nabla_b P. \quad \text{(C.5)}$$

Recall the normalization condition for the four-velocity,

$$u_b u^b = -1. \quad \text{(C.6)}$$

Operating on this equation with ∇_a yields

$$\nabla_a \left(u_b u^b \right) = u^b \nabla_a u_b + u_b \nabla_a u^b = 0, \quad \text{(C.7)}$$

or, since ∇_a is compatible with g^{ab},

$$u_b \nabla_a u^b = 0. \quad \text{(C.8)}$$

Using Eqs. (C.6) and (C.8) in Eq. (C.5), we find

$$\begin{aligned} u_a \nabla_b T^{ab} &= -u^b \nabla_b (\rho + P) - (\rho + P) \nabla_b u^b + u^b \nabla_b P \\ &= -u^b \nabla_b \rho - (\rho + P) \nabla_b u^b = 0, \end{aligned} \quad \text{(C.9)}$$

or, multiplying with u^a,

$$-u^a u^b \nabla_b \rho - (\rho + P) u^a \nabla_b u^b = 0. \quad \text{(C.10)}$$

We can now add Eq. (C.10) to our original equation for the divergence of T^{ab} (C.4) to obtain

$$u^a u^b \nabla_b P + (\rho + P) u^b \nabla_b u^a + \nabla^a P. \quad \text{(C.11)}$$

Since P is a scalar, we have $\nabla_b P = \partial_b P$ and $\nabla^a P = \partial^a P$. Making these substitutions in (C.11) and rearranging terms gives

$$(\rho + P) u^b \nabla_b u^a = -\partial^a P - u^a u^b \partial_b P, \quad \text{(C.12)}$$

which is the desired result.

Appendix D

Derivation of the entropy equation

In this appendix we derive the entropy equation,

$$d\left(\frac{\epsilon}{\rho_0}\right) = -Pd\left(\frac{1}{\rho_0}\right) \tag{D.1}$$

[cf. Eq. (3.6)], from the law of baryon conservation,

$$\nabla_a\left(\rho_0 u^a\right) = 0 \tag{D.2}$$

[cf. Eq. (3.2), and the conservation of energy-momentum,

$$\nabla_a T^{ab} = 0 \tag{D.3}$$

[cf. Eq. (3.3)]. We begin, as in our derivation of the relativistic Euler equation, by contracting Eq. (D.3) with the covariant four-velocity u_a. As shown in Appendix C, this yields

$$u_a \nabla_b T^{ab} = -u^b \nabla_b \rho - \left(\rho + P\right)\nabla_b u^b = 0. \tag{D.4}$$

[cf. Eq. (C.9)]. From the law of baryon conservation (D.2), we have

$$\nabla_a\left(\rho_0 u^a\right) = \rho_0 \nabla_a u^a + u^a \nabla_a \rho_0, \tag{D.5}$$

or

$$\nabla_a u^a = -\frac{1}{\rho_0} u^a \nabla_a \rho_0. \tag{D.6}$$

Making this substitution in Eq. (D.4) yields

$$u^b \nabla_b \rho = \frac{\rho + P}{\rho_0} u^b \nabla_b \rho_0. \tag{D.7}$$

We recognize that $u^b \nabla_b$ is equivalent to $d/d\tau$, where τ is the proper time as measured by an observer comoving with the fluid. We therefore have

$$\frac{d\rho}{d\tau} = \frac{\rho + P}{\rho_0} \frac{d\rho_0}{d\tau}, \tag{D.8}$$

or

$$\frac{d\rho}{d\rho_0} = \frac{\rho + P}{\rho_0} \tag{D.9}$$

[cf. Eq. (3.7)]. We will now show that Eq. (D.9) is equivalent to the entropy equation (D.1). We first use (3.1) to rewrite (D.9) as

$$d\rho = \frac{\rho + \varepsilon + P}{\rho_0} d\rho_0. \tag{D.10}$$

Multiplying both sides by $1/\rho_0$ and rearranging terms yields

$$\frac{1}{\rho_0} d\rho - \frac{1}{\rho_0} d\rho_0 - \frac{\varepsilon}{\rho_0^2} d\rho_0 = \frac{P}{\rho_0^2} d\rho_0, \tag{D.11}$$

or

$$\frac{1}{\rho_0} d\varepsilon - \frac{\varepsilon}{\rho_0^2} d\rho_0 = \frac{P}{d\rho_0^2} d\rho_0, \tag{D.12}$$

which we can write more compactly as

$$d\left(\frac{\varepsilon}{\rho_0}\right) = -P d\left(\frac{1}{\rho_0}\right). \tag{D.13}$$

Appendix E

Derivation of the relativistic fluid equations

In this appendix we derive the relativistic fluid equations (3.16) and (3.17) from the law of baryon conservation,

$$\nabla_a \left(\rho_0 u^a\right) = 0 \tag{E.1}$$

[cf. Eq. (3.2)], and the relativistic Euler equation,

$$\left(\rho + P\right) u^b \nabla_b u^a = -\partial^a P - u^a u^b \partial_b P \tag{E.2}$$

[cf. Eq. (3.5)], respectively. Here $u^a = \left(u^t, u^R, 0, 0\right)$ is the four-velocity of the fluid, ρ and ρ_0 are the total mass-energy density and rest-mass density, respectively, and P is the pressure. We choose to derive these equations in Schwarzschild coordinates, in which the line element is given by

$$ds^2 = -\left(1 - \frac{2M}{R}\right) dt^2 + \left(1 - \frac{2M}{R}\right)^{-1} dR^2 + R^2 d\Omega^2, \tag{E.3}$$

where t is the Schwarzschild time, R is the Schwarzschild radius, and M is the mass of the black hole.

E.1 The first fluid equation

We begin with the law of baryon conservation (E.1). Expanding the covariant derivative yields

$$\nabla_a \left(\rho_0 u^a\right) = \partial_a \left(\rho_0 u^a\right) + \rho_0 u^b \Gamma^a{}_{ab} = 0. \tag{E.4}$$

Since we are assuming steady-state flow, we have $\partial_t \rho_0 = \partial_t u^a = 0$. We can therefore rewrite the first term of (E.4) as

$$\partial_a \left(\rho_0 u^a\right) = \partial_R \left(\rho_0 u^R\right) = u^R \partial_R \rho_0 + \rho_0 \partial_R u^R. \tag{E.5}$$

We define $u = -u^R$ to be the inward velocity of the fluid. Eq. (E.5) then becomes

$$\partial_a \left(\rho_0 u^a\right) = -u \partial_R \rho_0 - \rho_0 \partial_R u = -\rho_0{}' u - \rho_0 u', \tag{E.6}$$

where in the last equality we have introduced $\rho_0{}' \equiv d\rho_0/dR$ and $u' \equiv du/dR$. In order to evaluate the last term in Eq. (E.4), we need to compute the Christoffel symbols $\Gamma^a{}_{bc}$ associated with the Schwarzschild metric (E.3). From the definition of $\Gamma^a{}_{bc}$,

$$\Gamma^a{}_{bc} = \frac{1}{2} g^{ad} \left(\partial_c g_{db} + \partial_b g_{dc} - \partial_d g_{bc}\right), \tag{E.7}$$

we obtain

$$\begin{aligned}
\Gamma^t{}_{tR} &= \frac{M}{R\left(R-2M\right)} \\
\Gamma^R{}_{tt} &= \frac{M}{R^3}\left(R-2M\right) \\
\Gamma^R{}_{RR} &= -\frac{M}{R\left(R-2M\right)} \\
\Gamma^R{}_{\theta\theta} &= -\left(R-2M\right) \\
\Gamma^R{}_{\phi\phi} &= -\left(R-2M\right)\sin^2\theta \\
\Gamma^\theta{}_{R\theta} &= \Gamma^\phi{}_{R\phi} = \frac{1}{R} \\
\Gamma^\theta{}_{\phi\phi} &= -\sin\theta\cos\theta
\end{aligned}$$

$$\Gamma^{\phi}{}_{\theta\phi} = \frac{\cos\theta}{\sin\theta}. \tag{E.8}$$

(Note that $\Gamma^{a}{}_{bc}$ are symmetric under exchange of the lower two indices: $\Gamma^{a}{}_{bc} = \Gamma^{a}{}_{cb}$.) We can now rewrite the last term in Eq. (E.4) as

$$\rho_0 u^b \Gamma^{a}{}_{ab} = \rho_0 u^R \Gamma^{a}{}_{aR} = -\rho_0 u \left(\Gamma^{t}{}_{tR} + \Gamma^{R}{}_{RR} + \Gamma^{\theta}{}_{\theta R} + \Gamma^{\phi}{}_{\phi R}\right), \tag{E.9}$$

or, since $\Gamma^{R}{}_{RR} = -\Gamma^{t}{}_{tR}$ and $\Gamma^{\theta}{}_{\theta R} = \Gamma^{\phi}{}_{\phi R} = 1/R$ [see Eq. (E.8)],

$$\rho_0 u^b \Gamma^{a}{}_{ab} = -\frac{2\rho_0 u}{R}. \tag{E.10}$$

Inserting (E.6) and (E.10) into (E.4), we obtain

$$-\rho_0{}' u - \rho_0 u' - \frac{2\rho_0 u}{R} = 0. \tag{E.11}$$

Dividing through by $-\rho_0 u$ yields

$$\frac{\rho_0{}'}{\rho_0} + \frac{u'}{u} + \frac{2}{R} = 0, \tag{E.12}$$

which is the desired result [cf. Eq. (3.16)].

E.2 The second fluid equation

We now turn our attention to the relativistic Euler equation (E.2). As above, we begin by expanding the covariant derivative. The left hand side then becomes

$$u^b \nabla_b u^a = u^b \left(\partial_b u^a + u^c \Gamma^{a}{}_{bc}\right). \tag{E.13}$$

Since we are assuming radial flow, the only non-vanishing spatial component of Eq. (E.2) is the $a = R$ component:

$$u^b \nabla_b u^R = u^b \left(\partial_b u^R + u^c \Gamma^{R}{}_{bc}\right), \tag{E.14}$$

Carrying out the sum over b and c yields

$$u^b \nabla_b u^R = u^t \left(\partial_t u^R + u^t \Gamma^R{}_{tt} \right) + u^R \left(\partial_R u^R + u^R \Gamma^R{}_{RR} \right). \tag{E.15}$$

In steady-state flow, we have $\partial_t u^R = 0$, so Eq. (E.15) simplifies to

$$u^b \nabla_b u^R = \left(u^t \right)^2 \Gamma^R{}_{tt} + \left(u^R \right)^2 \Gamma^R{}_{RR}. \tag{E.16}$$

Before we can evaluate the right side of (E.16), we need an expression for u^t, the time component of the fluid four-velocity. We can calculate u^t from the normalization condition $u_a u^a = -1$. This gives

$$-1 = g_{ab} u^a u^b = g_{tt} \left(u^t \right)^2 + g_{RR} \left(u^R \right)^2, \tag{E.17}$$

or, inserting our expressions for the metric coefficients [see Eq. (E.3)],

$$-1 = -\left(1 - \frac{2M}{R} \right) \left(u^t \right)^2 + \left(1 - \frac{2M}{R} \right)^{-1} \left(u^R \right)^2. \tag{E.18}$$

Substituting $u = -u^R$ and rearranging terms yields

$$\left(u^t \right)^2 = \frac{R}{R - 2M} \left(\frac{R}{R - 2M} u^2 + 1 \right) = \left(\frac{R}{R - 2M} \right)^2 \left(1 - \frac{2M}{R} + u^2 \right), \tag{E.19}$$

or

$$u^t = \pm \frac{R}{R - 2M} \left(1 - \frac{2M}{R} + u^2 \right)^{1/2}. \tag{E.20}$$

Both of these solutions are mathematically valid; in order to determine which one is physically relevant, we consider the limit $R \to \infty$. In this limit, we want $u^t = 1$, so we choose the positive solution,

$$u^t = \frac{R}{R - 2M} \left(1 - \frac{2M}{R} + u^2 \right)^{1/2}. \tag{E.21}$$

We can now insert (E.21) into (E.16) to obtain

$$u^b \nabla_b u^R = \left(\frac{R}{R-2M}\right)^2 \left(1 - \frac{2M}{R} + u^2\right) \frac{M}{R^3}\left(R - 2M\right) - \frac{M}{R\left(R-2M\right)} u^2 + uu', \quad \text{(E.22)}$$

or

$$u^b \nabla_b u^R = \frac{M}{R^2} + uu'. \quad \text{(E.23)}$$

We now have to deal with the right-hand side of Eq. (E.2). Since we are assuming spherically symmetric, radial flow, the only nonzero derivative of P is in the radial direction. We can therefore rewrite the first term on the right-hand side as

$$-\partial^R P = -g^{Ra}\partial_a P = -g^{RR}\partial_R P = -\left(1 - \frac{2M}{R}\right)\frac{dP}{dR} \quad \text{(E.24)}$$

and the second term as

$$-u^R u^b \partial_b P = -\left(u^R\right)^2 \partial_R P = -u^2 \frac{dP}{dR}. \quad \text{(E.25)}$$

Inserting (E.23), (E.24), and (E.25) into Eq. (E.2) yields

$$\left(\rho + P\right)\left(\frac{M}{R^2} + uu'\right) = -\frac{dP}{dR}\left(1 - \frac{2M}{R} + u^2\right), \quad \text{(E.26)}$$

or, dividing by $(\rho + P)$ and rearranging terms,

$$uu' = -\frac{1}{\rho + P}\frac{dP}{dR}\left(1 - \frac{2M}{R} + u^2\right) - \frac{M}{R^2}, \quad \text{(E.27)}$$

which is the desired result [cf. Eq. (3.20)].

Appendix F

Invariance of the fluid equations under the transformation $t = T + h(r)$

Consider the Schwarzschild solution in Schwarzschild coordinates

$$ds^2 = -f_0 dT^2 + f_0^{-1} dR^2 + R^2 d\Omega^2, \tag{F.1}$$

where T is the Schwarzschild time, R is the Schwarzschild radius, and

$$f_0 = f_0(R) = 1 - \frac{2M}{R}. \tag{F.2}$$

In the previous Appendix (Appendix E), we used this coordinate system to derive the relativistic fluid equations

$$\frac{{\rho_0}'}{\rho_0} + \frac{u'}{u} + \frac{2}{R} = 0 \tag{F.3}$$

and

$$uu' = -\frac{1}{\rho + P}\frac{dP}{dR}\left(1 - \frac{2M}{R} + u^2\right) - \frac{M}{R^2} \tag{F.4}$$

[cf. Eqs. (3.16) and (3.20), respectively]. Our goal here is to show that both of these equations are invariant under coordinate transformations of the form

$$t = T + h(R) \tag{F.5}$$

[cf. Eq. (4.5)], where the height function h depends on the radial coordinate only.

Let $h' \equiv dh/dR$. From (F.5), we have $dt = dT + h'dR$, or $dT = dt - h'dR$. In terms of the new time coordinate t, the line element (F.1) then becomes

$$ds^2 = -f_0 dt^2 + 2f_0 h' dt dR + \left(f_0^{-1} - f_0 h'^2\right) dR^2 + R^2 d\Omega^2. \tag{F.6}$$

In order to derive Eqs. (F.3) and (F.4), we will need the Christoffel symbols $\Gamma^a{}_{bc}$ associated with (F.6). From the definition of $\Gamma^a{}_{bc}$ [Eq. (E.7)], we obtain

$$\begin{aligned}
\Gamma^t{}_{tt} &= \frac{M}{R^2} f_0 h' \\
\Gamma^t{}_{tR} &= \frac{M}{R^2}\left(f_0^{-1} - f_0 h'^2\right) \\
\Gamma^t{}_{RR} &= -\frac{3M}{R} f_0 h' + \frac{M}{R^2} f_0^{-1} + \frac{1}{R^2} f_0 h'^3 - h'' \\
\Gamma^t{}_{\theta\theta} &= -R f_0 h' \\
\Gamma^t{}_{\phi\phi} &= -R f_0 h' \sin^2\theta \\
\Gamma^R{}_{tt} &= \frac{M}{R^2} f_0 \\
\Gamma^R{}_{tR} &= -\frac{M}{R^2} f_0 h' \\
\Gamma^R{}_{RR} &= -\frac{M}{R^2}\left(f_0^{-1} - f_0 h'^2\right) \\
\Gamma^R{}_{\theta\theta} &= -R f_0 \\
\Gamma^R{}_{\phi\phi} &= -R f_0 \sin^2\theta \\
\Gamma^\theta{}_{R\theta} &= \Gamma^\phi{}_{R\phi} = \frac{1}{R} \\
\Gamma^\theta{}_{\phi\phi} &= -\sin\theta\cos\theta \\
\Gamma^\phi{}_{\theta\phi} &= \frac{\cos\theta}{\sin\theta}.
\end{aligned} \tag{F.7}$$

F.1 The first fluid equation

As in Appendix E, we will derive the first fluid equation (F.3) from the law of baryon conservation,

$$\nabla_a \left(\rho_0 u^a\right) = 0 \tag{F.8}$$

[cf. Eq. (3.2)], where ρ_0 is the rest-mass density of the fluid and u^a is the four-velocity. As before, we assume radial fluid flow ($u^\theta = u^\phi = 0$) with inward velocity $u = -u^R$. We start by expanding the covariant derivative in (F.8). This gives

$$\nabla_a (\rho_0 u^a) = \partial_a (\rho_0 u^a) + \rho_0 u^b \Gamma^a{}_{ab} = u^a \partial_a \rho_0 + \rho_0 \partial_a u^a + \rho_0 u^b \Gamma^a{}_{ab}, \tag{F.9}$$

or, since ρ_0 and u both depend only on R,

$$\nabla_a (\rho_0 u^a) = u^R \partial_R \rho_0 + \rho_0 \partial_R u^R + \rho_0 u^b \Gamma^a{}_{ab} = -\rho_0{}' u + \rho_0 u' + \rho_0 u^b \Gamma^a{}_{ab}, \tag{F.10}$$

where we have substituted $u = -u^R$ and defined $\rho_0{}' \equiv \partial \rho_0 / \partial R$ and $u' \equiv \partial u / \partial R$. We now expand the sum in the last term to obtain

$$\begin{aligned} \rho_0 u^b \Gamma^a{}_{ab} &= \rho_0 u^t \Gamma^a{}_{at} + \rho_0 u^R \Gamma^a{}_{aR} \\ &= \rho_0 u^t \left(\Gamma^t{}_{tt} + \Gamma^R{}_{Rt} \right) + \rho_0 u^R \left(\Gamma^t{}_{tR} + \Gamma^R{}_{RR} + \Gamma^\theta{}_{\theta R} + \Gamma^\phi{}_{\phi R} \right). \end{aligned} \tag{F.11}$$

From Eq. (F.7), we have $\Gamma^R{}_{Rt} = -\Gamma^t{}_{tt}$ and $\Gamma^R{}_{RR} = -\Gamma^t{}_{tR}$, so

$$\rho_0 u^b \Gamma^a{}_{ab} = \rho_0 u^R \left(\Gamma^\theta{}_{\theta R} + \Gamma^\phi{}_{\phi R} \right) = -\frac{2\rho_0 u}{R}, \tag{F.12}$$

and (F.8) becomes

$$-\rho_0{}' u - \rho_0 u' - \frac{2\rho_0 u}{R} = 0. \tag{F.13}$$

Dividing through by $-\rho_0 u$ gives

$$\frac{\rho_0{}'}{\rho_0} + \frac{u'}{u} + \frac{2}{R} = 0, \tag{F.14}$$

which is the desired result [cf. Eq. (F.3)].

F.2 The second fluid equation

We will derive the second fluid equation (F.4) from the relativistic Euler equation,

$$(\rho + P)\, u^b \nabla_b u^a = \partial^a P - u^a u^b \partial_b P \tag{F.15}$$

[cf. Eq. (3.5)]. Here $\rho = \rho_0 + \epsilon$ is the total mass-energy density of the fluid and P is the pressure. We evaluate (F.15) for $a = R$, since this is the only component that will yields a nontrivial result. Expanding the covariant derivative on the left-hand side then gives

$$\begin{aligned} u^b \nabla_b u^R &= u^t \left(\partial_t u^R + u^a \Gamma^R{}_{at}\right) + u^R \left(\partial_R u^R + u^a \Gamma^R{}_{aR}\right) \\ &= u^t \left(u^t \Gamma^R{}_{tt} + u^R \Gamma^R{}_{Rt}\right) + u^R \left(\partial_R u^R + u^t \Gamma^R{}_{tR} + u^R \Gamma^R{}_{RR}\right) \\ &= \left(u^t\right)^2 \Gamma^R{}_{tt} + 2u^t u^R \Gamma^R{}_{tR} + \left(u^R\right)^2 \Gamma^R{}_{RR} + u^R \partial_R u^R. \end{aligned} \tag{F.16}$$

As in Appendix E, we compute u^t from the normalization of the four-velocity, $u_a u^a = -1$. This gives

$$\begin{aligned} -1 &= g_{ab} u^a u^b \\ &= g_{tt} \left(u^t\right)^2 + 2 g_{tr} u^t u^r + g_{rr} \left(u^r\right)^2 \\ &= -f_0 \left(u^t\right)^2 - 2 f_0 h' u u^t + \left(f_0^{-1} - f_0 h'^2\right) u^2, \end{aligned} \tag{F.17}$$

or

$$f_0 \left(u^t\right)^2 + 2 f_0 h' u u^t - \left(f_0^{-1} - f_0 h'^2\right) u^2 - 1 = 0. \tag{F.18}$$

We can now solve for u^t using the quadratic formula:

$$\begin{aligned} u^t &= \frac{1}{2 f_0} \left[-2 f_0 h' u \pm \sqrt{4 f_0^2 h'^2 u^2 + 4 f_0 \left(\left(f_0^{-1} - f_0 h'^2\right) u^2 + 1\right)}\right] \\ &= \frac{1}{2 f_0} \left[-2 f_0 h' u \pm \sqrt{4 f_0 + 4 u^2}\right] \\ &= -h' u \pm f_0^{-1} \sqrt{f_0 + u^2}. \end{aligned} \tag{F.19}$$

We want $u^t = 1$ in the limit $r \to \infty$ ($u \to 0$), so we choose the positive solution:

$$u^t = -h'u + f_0^{-1}\sqrt{f_0 + u^2}. \tag{F.20}$$

We are now ready to evaluate each of the terms in (F.16). The first term becomes

$$\begin{aligned}
\left(u^t\right)^2 \Gamma^R{}_{tt} &= \left[-h'u + f_0^{-1}\sqrt{f_0+u^2}\right]^2 \frac{M}{R^2} f_0 \\
&= \left[h'^2u^2 - 2f_0^{-1}h'u\sqrt{f_0+u^2} + f_0^{-2}\left(f_0+u^2\right)\right]\frac{M}{R^2}f_0 \\
&= \frac{M}{R^2}f_0h'^2u^2 - \frac{2M}{R^2}h'u\sqrt{f_0+u^2} + \frac{M}{R^2} + \frac{M}{R^2}f_0^{-1}u^2,
\end{aligned} \tag{F.21}$$

the second

$$\begin{aligned}
2u^tu^R\Gamma^R{}_{tR} &= 2\left[-h'u + f_0^{-1}\sqrt{f_0+u^2}\right]\frac{M}{R^2}f_0h'u \\
&= -\frac{2M}{R^2}f_0h'^2u^2 + \frac{2M}{R^2}h'u\sqrt{f_0+u^2},
\end{aligned} \tag{F.22}$$

the third

$$\left(u^R\right)^2\Gamma^R{}_{RR} = u^2\left[-\frac{M}{R^2}\left(f_0^{-1} - f_0h'^2\right)\right] = -\frac{M}{R^2}f_0^{-1}u^2 + \frac{M}{R^2}f_0h'^2u^2, \tag{F.23}$$

and the last term is simply

$$u^R\partial_R u^R = uu'. \tag{F.24}$$

When we insert Eqs. (F.21), (F.22), (F.23), and (F.24) back into (F.16), we find that many terms cancel, and we are left with

$$u^b\nabla_b u^R = (\rho + P)\left(\frac{M}{R^2} + uu'\right). \tag{F.25}$$

We now turn our attention to the right hand side of Eq. (F.15). The first term can be rewritten as

$$\partial^R P = g^{RR}\partial_R P = f_0\partial_R P = -f_0\frac{dP}{dR}, \tag{F.26}$$

and the second term as

$$u^R u^b \partial_b P = \left(u^R\right)^2 \partial_R P = u^2 \frac{dP}{dR}. \tag{F.27}$$

The entire right-hand side then becomes

$$-\partial^R P - u^r u^b \partial_b P = -\frac{dP}{dR}\left(f_0 + u^2\right). \tag{F.28}$$

Substituting Eqs. (F.25) and (F.28) into (F.15) yields

$$(\rho + P)\left(\frac{M}{r^2} + uu'\right) = -\frac{dP}{dr}\left(f_0 + u^2\right), \tag{F.29}$$

or

$$uu' = -\frac{1}{\rho + P}\frac{dP}{dr}\left(f_0 + u^2\right) - \frac{M}{r^2} = -\frac{1}{\rho + P}\frac{dP}{dr}\left(1 - \frac{2M}{r} + u^2\right) - \frac{M}{r^2}, \tag{F.30}$$

which is the desired result [cf. Eq. (F.4)].

We have thus shown that Eqs. (F.3) and (F.4) are invariant under coordinate transformations of the form $t = T + h\,(R)$.

Appendix G

Computing K_{ij} in maximal and analytical trumpet coordinates

In this appendix we compute the components of the extrinsic curvature K_{ij} for maximally sliced and analytical trumpet coordinates. We can calculate K_{ij} from the spatial metric, lapse, and shift vector:

$$K_{ij} = \frac{1}{2\alpha} \left(-\partial_t \gamma_{ij} + D_i \beta_j + D_j \beta_i \right) \tag{G.1}$$

[cf. Eq. (4.21)]. Here D_i denotes the covariant derivative associated with the spatial metric, defined as

$$D_i \equiv \partial_i \beta_j - \beta_k \Gamma^k ij, \tag{G.2}$$

where

$$\Gamma^k ij \equiv \frac{1}{2} \gamma^{kl} \left(\partial_j \gamma_{li} + \partial_i \gamma_{lj} - \partial_l \gamma_{ij} \right) \tag{G.3}$$

are the three-dimensional connection coefficients.

G.1 Maximal trumpets

In maximal trumpet coordinates, the spatial metric is

$$\gamma_{ij} = \psi^4 \eta_{ij} = \left(\frac{R}{r} \right)^2 \mathrm{diag} \left(1, r^2, r^2 \sin^2 \theta \right), \tag{G.4}$$

where we have expressed ψ using Eq. (4.35). Since γ_{ij} is diagonal, the inverse metric is simply

$$\gamma^{ij} = \psi^{-4}\eta^{ij} = \left(\frac{r}{R}\right)^2 \mathrm{diag}\left(1, r^{-2}, r^{-2}\sin^{-2}\theta\right). \tag{G.5}$$

Using Eq. (G.3) we find that the nonzero connection coefficients in these coordinates are

$$\begin{aligned}
\Gamma^r{}_{rr} &= \frac{\psi^2}{R}(f-1) \\
\Gamma^r{}_{\theta\theta} &= -\frac{fR^2}{\psi^2} \\
\Gamma^r{}_{\phi\phi} &= -\frac{fR^2}{\psi^2}\sin\theta \\
\Gamma^\theta{}_{r\theta} &= \Gamma^\phi{}_{r\phi} = \frac{\psi^2 f}{R} \\
\Gamma^\theta{}_{\phi\phi} &= -\cos\theta\sin\theta \\
\Gamma^\phi{}_{\theta\phi} &= \frac{\cos\theta}{\sin\theta}.
\end{aligned} \tag{G.6}$$

We also need the covariant form of the shift vector:

$$\beta_r = \gamma_{ri}\beta^i = \gamma_{rr}\beta^r = \frac{\psi^2 C}{R^2}. \tag{G.7}$$

In both maximal and analytical trumpet coordinates, the spatial metric is time-independent ($\partial_t \gamma_{ij} = 0$), so

$$K_{ij} = \frac{1}{2\alpha}\left(D_i\beta_j + D_j\beta_i\right). \tag{G.8}$$

We find that the only nonzero components of K_{ij} are the diagonal components, K_{rr}, $K_{\theta\theta}$, and $K_{\phi\phi}$. From Eq. (G.8), we have

$$K_{rr} = \frac{1}{\alpha}D_r\beta_r = \frac{1}{\alpha}\left(\partial_r\beta_r - \beta_k\Gamma^k{}_{rr}\right). \tag{G.9}$$

Consider the two terms in parentheses separately. Using the relation between R and r, we can rewrite β_r as

$$\beta_r = \frac{\psi^2 C}{R^2} = \frac{C}{Rr}. \tag{G.10}$$

Then the first term in (G.9) becomes

$$\partial_r \beta_r = \frac{\partial}{\partial r}\left(\frac{C}{Rr}\right) = -\frac{C}{R^2 r}\left(\frac{\partial R}{\partial r} + \frac{R}{r}\right) = -\frac{C}{R^2 r}\left(\psi^2 f + \psi^2\right) = -\frac{\psi^2 C}{R^2 r}\left(f+1\right). \quad \text{(G.11)}$$

For the second term, we have

$$\beta_r \Gamma^r{}_{rr} = \frac{\psi^4 C}{R^3}\left(f-1\right). \quad \text{(G.12)}$$

Substituting (G.11) and (G.12) into (G.9) yields

$$K_{rr} = \frac{1}{f}\left[-\frac{\psi^4 C}{R^3}\left(f+1\right) - \frac{\psi^4 C}{R^3}\left(f-1\right)\right] = -\frac{2\psi^4 C}{R^3} \quad \text{(G.13)}$$

We now want to compute $K_{\theta\theta}$ and $K_{\phi\phi}$. Since $\beta_\theta = \beta_\phi = 0$, we have

$$K_{\theta\theta} = \frac{1}{\alpha}\left(\partial_\theta \beta_\theta - \beta_k \Gamma^k{}_{\theta\theta}\right) = -\frac{1}{\alpha}\beta_r \Gamma^r{}_{\theta\theta} = \frac{C}{R}, \quad \text{(G.14)}$$

and

$$K_{\phi\phi} = \frac{1}{\alpha}\left(\partial_\phi \beta_\phi - \beta_k \Gamma^k{}_{\phi\phi}\right) = -\frac{1}{\alpha}\beta_r \Gamma^r{}_{\phi\phi} = \frac{C}{R}\sin\theta \quad \text{(G.15)}$$

[cf. Eq. (4.41)]. Finally, since maximal trumpet coordinates represent a maximal slicing of the Schwarzschild spacetime, we should find $K = 0$ in these coordinates. Using the above expressions for the components of K_{ij}, we have

$$K \equiv \gamma^{ij} K_{ij} = \gamma^{rr} K_{rr} + \gamma^{\theta\theta} K_{\theta\theta} + \gamma^{\phi\phi} K_{\phi\phi} = -\frac{2C}{R^3} + \frac{C}{R^3} + \frac{C}{R^3} = 0. \quad \text{(G.16)}$$

G.2 Analytical trumpets

We now repeat the above calculation in analytical trumpet coordinates. In these coordinates, the spatial metric is

$$\gamma_{ij} = \psi^4 \eta_{ij} = \left(1 + \frac{R_0}{r}\right)^2 \mathrm{diag}\left(1, r^2, r^2 \sin^2\theta\right), \quad \text{(G.17)}$$

and the inverse metric is

$$\gamma^{ij} = \left(1 + \frac{R_0}{r}\right)^{-2} \mathrm{diag}\left(1, r^{-2}, r^{-2}\sin^{-2}\theta\right). \tag{G.18}$$

From Eq. (G.3) we find the nonzero three-dimensional connection coefficients

$$\begin{aligned}
\Gamma^r{}_{rr} &= -\frac{R_0}{r\left(r + R_0\right)} \\
\Gamma^r{}_{\theta\theta} &= -\frac{r^2}{r + R_0} \\
\Gamma^r{}_{\phi\phi} &= -\frac{r^2\sin^2\theta}{r + R_0} \\
\Gamma^\theta{}_{r\theta} &= \Gamma^\phi{}_{r\phi} = \frac{1}{r + R_0} \\
\Gamma^\theta{}_{\phi\phi} &= -\cos\theta\sin\theta \\
\Gamma^\phi{}_{\theta\phi} &= \frac{\cos\theta}{\sin\theta}.
\end{aligned} \tag{G.19}$$

The covariant form of the shift vector is

$$\beta_r = \gamma_{rj}\beta^j = \gamma_{rr}\beta^r = \left(1 + \frac{R_0}{r}\right)^2 \frac{f_1 r}{\left(r + R_0\right)^2} = \frac{f_1}{r}. \tag{G.20}$$

Once again, we find that the only nonzero components of the extrinsic curvature are the diagonal components. From Eq. (G.8), we again have

$$K_{rr} = \frac{1}{\alpha}\left(\partial_r\beta_r - \beta_k\Gamma^k{}_{rr}\right). \tag{G.21}$$

We can use the definition of f_1 [Eq. (4.47)] to rewrite the first term in parentheses as

$$\begin{aligned}
\frac{\partial}{\partial r}\beta_r &= \frac{\partial}{\partial r}\left[\frac{\left(2r\left(M - R_0\right) + R_0\left(2M - R_0\right)\right)^{1/2}}{r}\right] \\
&= \frac{M - R_0}{r\left[2r\left(M - R_0\right) + R_0\left(2M - R_0\right)\right]^{1/2}} - \frac{\left[2r\left(M - R_0\right) + R_0\left(2M - R_0\right)\right]^{1/2}}{r^2} \\
&= \frac{M - R_0}{f_1 r} - \frac{f_1}{r^2}.
\end{aligned} \tag{G.22}$$

For the second term, we have

$$\beta_k \Gamma^k{}_{rr} = \beta_r \Gamma^r{}_{rr} = \frac{f_1 R_0}{r^2 (r + R_0)}. \tag{G.23}$$

Inserting (G.22) and (G.23) into Eq. (G.21) yields

$$K_{rr} = \frac{r + R_0}{r} \left[\frac{M - R_0}{f_1 r} - \frac{f_1}{r^2} + \frac{f_1 R_0}{r^2 (r + R_0)} \right], \tag{G.24}$$

Reinserting Eq. (4.47) for f_1 and simplifying gives our final result,

$$K_{rr} = -\frac{r (M - R_0) + M R_0}{f_1 r^2}. \tag{G.25}$$

We now compute the two other diagonal components, $K_{\theta\theta}$ and $K_{\phi\phi}$. We again have $\beta_\theta = \beta_\phi = 0$, so Eq. (G.21) yields

$$K_{\theta\theta} = -\frac{1}{\alpha} \beta_r \Gamma^r{}_{\theta\theta} = f_1 \tag{G.26}$$

and

$$K_{\phi\phi} = -\frac{1}{\alpha} \beta_r \Gamma^r{}_{\phi\phi} = f_1 \sin^2 \theta. \tag{G.27}$$

[cf. Eq. (4.53)]. We can also combine Eqs. (G.25), (G.26), and (G.27) to obtain an expression for the mean curvature K. From the definition of the mean curvature, we have

$$\begin{aligned} K &= \gamma^{rr} K_{rr} + \gamma^{\theta\theta} K_{\theta\theta} + \gamma^{\phi\phi} K_{\phi\phi} \\ &= \left(1 + \frac{R_0}{r} \right)^{-2} \left[-\frac{r (M - R_0) + M R_0}{f_1 r^2} + \frac{2 f_1}{r^2} \right], \end{aligned} \tag{G.28}$$

or

$$K = \frac{(3r + 2R_0)(M - R_0) + M R_0}{f_1 (r + R_0)^2} \tag{G.29}$$

[cf. Eq. (4.54)].

References

[1] M. A. Abramowicz and P. C. Fragile. Foundations of Black Hole Accretion Disk Theory. *Living Rev. Relativity*, 16:1, 2013.

[2] F. C. Michel. Wormhole initial conditions. *Ap. Space Sci.*, 15:153, 1972.

[3] M. C. Begelmann. Black holes in radiation-dominated gas: an analogue of the Bondi accretion problem. *Mon. Not. R. Astron. Soc.*, 184:53–67, 1978.

[4] S. L. Shapiro and S. A. Teukolsky. *Black Holes, White Dwarfs, and Neutron Stars: the Physics of Compact Objects*. Wiley Interscience, New York, 1983.

[5] J. F. Hawley, L. L. Smarr, and J. R. Wilson. A numerical study of nonspherical black hole accretion. I. Equations and test problems. *Astrophys. J.*, 277:396–311, 1984.

[6] J. F. Hawley, L. L. Smarr, and J. R. Wilson. A numerical study of nonspherical black hole accretion. II. Finite differencing and code calibration. *Astrophys. J. Suppl.*, 55:211–246, 1984.

[7] J.-P. De Villiers and J. F. Hawley. A numerical method for general relativistic magnetohydrodynamics. *Astrophys. J.*, 589:458–480, 2003.

[8] C. F. Gammie, J. C. McKinney, and G. Tóth. HARM: a numerical scheme for general relativistic magnetohydrodynamics. *Astrophys. J.*, 589:444–457, 2003.

[9] M. D. Duez, Y. T. Liu, S. L. Shapiro, and B. C. Stephens. Relativistic magnetohydrodynamics in dynamical spacetimes: Numerical methods and tests. *Phys. Rev. D*, 72:024028/1–21, 2005.

[10] J. A. Faber, T. W. Baumgarte, Z. B. Etienne, S. L. Shapiro, and K. Taniguchi. Relativistic hydrodynamics in the presence of puncture black holes. *Phys. Rev. D*, 76:104021/1–21, 2007.

[11] P. Mösta, B. C. Mundin, J. A. Faber, R. Haas, S. C. Noble, T. Bode, F. Löffler, C. D. Ott, C. Reisswig, and E. Schnetter. GRHydro: a new open-source general-relativistic mangetohydrodynamics code for the einstein toolkit. *Class. Quantum Grav.*, 31:015005, 2014.

[12] F. Pretorius. Evolution of binary black-hole spacetimes. *Phys. Rev. Lett.*, 95:121101/1–4, 2005.

[13] M. Campanelli, C. O. Lousto, P. Marronetti, and Y. Zlochower. Accurate evolutions of orbiting black-hole binaries without excision. *Phys. Rev. Lett.*, 96:111101/1–4, 2006.

[14] J. G. Baker, J. Centrella, D.-I. Choi, M. Koppitz, and J. van Meter. Gravitational-wave extraction from an inspiraling configuration of merging black holes. *Phys. Rev. Lett.*, 96:111102/1–4, 2006.

[15] T. Nakamura, K. Oohara, and Y. Kojima. General relativistic collapse to black holes and gravitational waves from black holes. *Prog. Theor. Phys. Suppl.*, 90:1–218, 1987.

[16] M. Shibata and T. Nakamura. Evolution of three-dimensional gravitational waves: Harmonic slicing case. *Phys. Rev. D*, 52:5428–5444, 1995.

[17] T. W. Baumgarte and S. L. Shapiro. Numerical integration of Einstein's field equations. *Phys. Rev. D*, 59:024007/1–7, 1998.

[18] C. Bona, J. Massó, E. Seidel, and J. Stela. New Formalism for Numerical Relativity. *Phys. Rev. Lett.*, 75:600–603, 1995.

[19] M. Alcubierre, B. Brügmann, P. Diener, M. Koppitz, D. Pollney, E. Seidel, and R. Takahashi. Gauge conditions for long-term numerical black hole evolutions without excision. *Phys. Rev. D*, 67:084023, 2003.

[20] M. Hannam, S. Husa, D. Pollney, B. Bruegmann, and N. O'Murchadha. Geometry and Regularity of Moving Punctures. *Phys. Rev. Lett.*, 99:241102/1–4, 2007.

[21] M. Hannam, S. Husa, F. Ohme, B. Brügmann, and N. Ó Murchadha. Wormholes and trumpets: the Schwarzschild spacetime for the moving-puncture generation. *Phys. Rev. D*, 78:064020/1–19, 2008.

[22] T. W. Baumgarte and S. L. Shapiro. *Numerical relativity: Solving Einstein's equations on the computer*. Cambridge University Press, Cambridge, 2010.

[23] K. A. Dennison and T. W. Baumgarte. A simple family of analytical trumpet slices of the Schwarzschild spacetime. *Class. Quantum Grav.*, 31:117001, 2014.

[24] H. Bondi. On spherically symmetric accretion. *Mon. Not. R. Astron. Soc.*, 112:195–204, 1952.

[25] T. W. Baumgarte, P. J. Montero, and E. Müller. Numerical relativity in spherical polar coordinates: Off-center simulations. *Phys. Rev. D*, 91:064035/1–14, 2015.

[26] T. W. Baumgarte and S. G. Naculich. Analytical representation of a black hole puncture solution. *Phys. Rev. D*, 75:067502/1–4, 2007.

[27] M. Hannam, S. Husa, N. Ó Murchadha, B. Brügmann, J. A. González, and U. Sperhake. Where do moving punctures go? *J. Phys. Conf. Series*, 66:012047/1–9, 2007.

[28] T. W. Baumgarte, P. J. Montero, I. Cordero-Carrión, and E. Müller. Numerical relativity in spherical polar coordinates: evolution calculations with the bssn formulation. *Phys. Rev. D*, 87:044026/1–14, 2013.

[29] P. J. Montero, T. W. Baumgarte, and E. Müller. General relativistic hydrodynamics in curvilinear coordinates. *Phys. Rev. D*, 89:084043/1–15, 2014.

[30] J. David Brown. Covariant formulations of Baumgarte, Shapiro, Shibata and Nakamura and the standard gauge. *Phys. Rev. D*, 79:104029/1–6, 2009.

[31] E. Gourgoulhon. *3+1 formalism in general relativity*. Springer, New York, 2012.